Morphological characterization and reconstruction of fractured heat-treated glass

Yuhan Zhu[a,b], Jian Yang[a,b], Xing-er Wang[a,b*], Dongdong Xie[a,b], Xiaonan Hou[c]

[a] State Key Laboratory of Ocean Engineering, Shanghai Jiao Tong University, Shanghai 200240, PR China

[b] Shanghai Key Laboratory for Digital Maintenance of Buildings and Infrastructure, School of Naval Architecture, Ocean and Civil Engineering, Shanghai Jiao Tong University, Shanghai 200240, PR China

[c] School of Engineering, Lancaster University, Lancaster, LA1 4YW, UK

Abstract: Fracture morphology has insightful information related to the residual effect of fractured structural glass, which is vital in assessing the post-fracture performance of glass members. This study experimentally characterized the fracture morphology of heat-treated glass and developed a novel method of morphology reconstruction, which aims to facilitate the numerical analysis of fractured structural glass. With the development of a computer-vision-based method for transparent objects, the morphology information from fragmentation tests was extracted and systematically investigated for monolithic heat-treated glass with various thicknesses, surface compressive stresses and fracture initiation locations, which are considered as the key influencing factors of heat-treated glass fracture. The geometrical features of fragments and their spatial distribution were quantitatively analysed, identifying their correlations with glass properties. The result indicates that the distribution of fragment centroids shows greater dispersion as the tempering level increases, and the fragments tend to be smaller and more rounded. The strain energy release at fracture was also assessed by fracture patterns, showing it presents high sensitivity to the glass thickness and surface compressive stress. Subsequently, a novel approach was proposed for the stochastic reconstruction of fracture morphology, combining feature points distribution and Voronoi tessellation concept. The control parameters are determined by data from the fragmentation tests and the influence of fracture load could be properly considered. The proposed method shows satisfactory outcomes and good agreement with the experimental records, which has further potential in developing refined numerical models by considering more realistic fracture morphology of glass members.

Keywords: Heat-treated glass; Thermally tempered glass; Fracture morphology; Surface compressive stress; Spatial distribution; Voronoi tessellation.

1. Introduction

Although structural glass, mostly in the form of laminated glass, has been increasingly used in modern architectures [1, 2], safety concern still arises as glass may have sudden failure due to its brittleness [3, 4]. Different factors such as external loads [5, 6] and internal defects [7-9] can result in the fracture of glass layer, which significantly damages the load capacity of structural glass. In engineering practice, damaged glass members are unlikely to have an immediate replacement and might sustain further destructive load, *e.g.*, projectile impact in windstorms [10] and multiple blasts in terrorist attacks [11]. Therefore, it is of great importance to consider the post-fracture state of glass members in the design.

In past practice, the sacrificial ply concept is widely adopted in the design of structural glass in post-fracture state. It assumes the glass layer carrying live load to be broken and excludes the residual effect of the fractured layer on the post-fracture performance of glass members [12, 13]. However, this concept results in more consumption of materials and higher costs. It also neglects several negative effects due to the glass fracturing, *e.g.*, the out-of-plane deformation by the expansion of fractured glass which further weakens the load-bearing ability. Furthermore, the fractured glass layer can also yield residual effects on the post-fracture ability of glass members from the following aspects: (a) Fragments are interlocked with neighbouring ones to maintain integrity under the constraints of the interlayer, the cracked glass layer can hence remain a certain load capacity; (b) Fragments bonded to the interlayer can provide tension stiffening effect, which can enhance the post-fracture stiffness [14, 15]; (c) Certain fragment geometry may lead to the localized tearing of the interlayer and facilitate the structural failure [16]; (d) Secondary cracking of large fragments may have unfavourable consequences, including ejection hazard and reduction of load capacity [17, 18]. Thus, the influence of the fractured glass layer should be carefully introduced in cases with significant post-fracture consequences.

By the adhesion to the interlayer, fractured glass layer can still contribute to the residual load capacity of the laminated glass members. It is natural to consider the fracture morphology as a nonnegligible factor, which has been proven by the experimental findings of Zhao et al. [19], showing that the laminated glass with different fracture morphologies had significantly different post-fracture performances.

Preliminary investigations have been conducted on the fracture propagation and morphology of glasses with different strengthened techniques. Nielsen et al. [20] identified the propagation and branching principle of cracks according to the observation about the fracture process of thermally tempered glass. Their works subsequently gave the relationship between surface compressive stress and fragments number using fragmentation test [21] as well as that between strain energy and fracture morphology [22, 23]. Bradt [24] concluded the importance of the internal and external energy in fracturing development by observing the fracture patterns of glass objects. Tang et al. [25] pointed out that the fracture process and final morphology of chemically strengthened glass were affected by the elastic energy stored inside, which can be correlated to the central tensile stress. Lee et al. [26] also found that the glass thickness and tempering level, which are closely related to the stored energy of glass, had a strong relationship with the fragmentation behaviour. From the studies above, it can be seen that the fracture process is affected by the internal energy status of glass materials. According to the theory of glass strengthening, internal strain energy storage is externally correlated to glass thickness and surface compressive stress, which can be acquired directly. Thus, potential factors including glass thickness and tempering level should be considered in the analysis of fracture morphology.

Limited works on the description and characterization of fracture morphology can be found so far. Dugnani et al. [27] proposed an analytical model to describe the crack evolution of tempered glass, which can estimate the fragment size with various thicknesses and surface compressive stresses. Molnár et al. [28] developed a theoretical method to describe the propagation of glass fracture, which used Voronoi tessellation for the estimation of crack length. Pourmoghaddam et al. [29, 30] introduced Voronoi tessellation to predict the fragmentation of tempered glass. Wang et al. [16, 31] developed refined numerical models to investigate the post-fracture performance of laminated glass, of which the fracture morphology was involved and generated using Voronoi tessellation with customized generation parameters. Current attempts at Voronoi tessellation show its potential in generating the fracture morphology of glass. However, more in-depth and comprehensive investigations into the statistical and spatial features of morphological parameters are required to obtain applicable parameters and procedures to reconstruct accurate fracture patterns.

This study focuses on the experimental characterization and virtual reconstruction of glass fracture morphology. The heat-treated glass dominating the use of structural glass in the

construction was considered. Experimental characterization encompasses the fragmentation tests and the feature analysis of morphological parameters. The former tested 81 glass specimens, which were devised with multiple influencing factors, to obtain a dataset of morphological images. A computer-vision-based method was employed to extract the geometrical characteristics from the dataset. A comprehensive study on the statistical and spatial features of glass fracture morphology from multiple perspectives was subsequently conducted, which obtained the parameters for reconstructing more realistic morphology. Finally, a stochastic reconstruction method on the basis of the proposed feature points distribution approach and the concept of Voronoi tessellation was developed.

2. Fragmentation tests

Fragmentation tests were performed to collect the morphological images of fractured heat-treated glass. Three key factors, *i.e.*, glass thickness, surface compressive stress and fracture initiation point, were adopted to identify their influences on the fracture morphology.

2.1 Testing specimens

In this study, 81 monolithic glass specimens in nine groups were manufactured and tested. The plane dimension of specimens was determined to be 600 mm × 300 mm. The nominal thicknesses of the specimens were 6, 8 and 12 mm, which were frequently used in practice. The glass specimen was without surface treatment and had edge treatments including polishing before tempering. The glass specimens were manufactured by Henan Zhongbo Glass Co., Ltd following the specific requirement of this study. Each group had three levels of surface compressive stress, which were achieved by adjusting the tempering procedure. The average incremental stress between neighbouring groups was required to be greater than 10 MPa, which can guarantee that the corresponding fracture morphologies present adequate differences.

The actual glass thickness and surface compressive stress of specimens, which can be used to estimate the elastic strain energy of heat-treated glass, were recorded before testing. Glass thickness was measured at the midpoints of two perpendicular edges (points a and b in **Fig. 1**). The surface compressive stress σ_s was measured at four testing points (see points 1 to 4 in **Fig. 1**) by surface stress meter (type JF-1E). The recorded data of glass thickness and surface compressive stress was

listed in **Table 1** and **Table 2**, respectively. The arithmetic mean (avg.) as well as the standard deviation (std.) of the measured data were calculated, showing that the specimen thickness and surface compressive stress within the same group have good uniformity. The deviation rate in **Table 1** shows that the actual measured value is close to the nominal value. **Table 2** also gives other general information of testing specimens. It should be clarified that, as for the specimen number, two digits after "M" represent the nominal glass thickness; *a*, *b*, *c* refer to low, medium and high tempering levels, respectively. The last optional digit denotes the fracture initiation point.

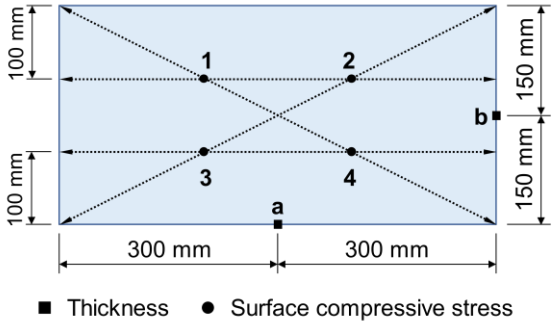

Fig. 1 Distribution of measurement points

Table 1 Thickness of monolithic heat-treated glass specimens

Nominal thickness (mm)	Avg. of actual thickness (mm)	Std. of glass thickness (mm)	Deviation rate (%)
6	5.88	0.037	2.03
8	7.92	0.045	0.99
12	11.93	0.033	0.60

Table 2 General information of monolithic heat-treated glass specimens

Specimen No.	Thickness (mm)	Dimension (mm × mm)	Tempering level	Avg. of σ_s (MPa)	Std. of σ_s (MPa)	Specimen quantity
M06a(1/2/3)	6	600 × 300	low	76.82	1.89	9
M06b(1/2/3)	6	600 × 300	medium	91.50	1.17	9
M06c(1/2/3)	6	600 × 300	high	103.41	2.12	9
M08a(1/2/3)	8	600 × 300	low	69.53	1.03	9
M08b(1/2/3)	8	600 × 300	medium	84.56	1.47	9
M08c(1/2/3)	8	600 × 300	high	103.70	1.42	9
M12a(1/2/3)	12	600 × 300	low	60.80	1.08	9
M12b(1/2/3)	12	600 × 300	medium	71.09	1.33	9
M12c(1/2/3)	12	600 × 300	high	94.20	2.49	9

2.2 Testing procedure

To facilitate the efficiency of image acquisition, the glass specimens were placed vertically and

fixed by the testing apparatus shown in **Fig. 2** (a). Because of the transparency of glass material, it is difficult to identify the fracture morphology directly using camera system. The testing apparatus was devised to generate and enhance the projection of fracture morphology on a polycarbonate plate behind the glass specimen. A high-resolution industrial camera (type MV-SUA2000C-T) was then used to collect the morphological images of fractured specimens on the polycarbonate plate. A computer-vision-based method was employed to process and extract the featured information of fracture morphology with the open source computer vision library OpenCV [32], following the procedures in **Fig. 3**. In this workflow, the original photos from the industrial camera are first pre-processed to obtain usable images of the fractured glass. Due to the lens distortion of camera and the inevitable inclusion of redundant environmental information in the images obtained from direct photography, distortion correcting and extraneous information cropping must be performed on the original images before identifying fracture morphology. Then the images are further processed with a series of pixel-based operations, including the thresholding method and morphological operation, to identify and extract the locations of cracks. For the output preliminary figures of the fracture morphology, optimization algorithm is designed to eliminate irrational information therein, *e.g.*, isolated lines and closed areas that are significantly too small. The final obtained fracture morphology can be used for data collection and feature analysis.

A drill with sharp diamond tip was used to crack the specimens. Three fracture initiation points at corner (1), midpoint (2) of long edge and the centre (3) were set (**Fig. 2** (b)) to capture the associated influences on fracture morphology.

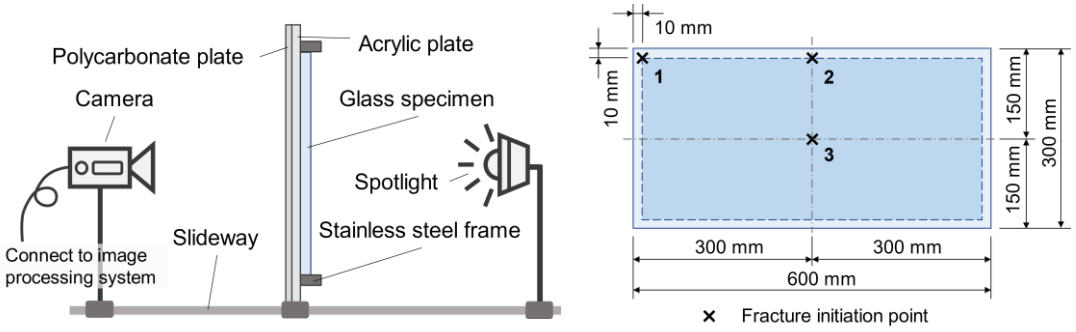

(a) Schematic of the experimental setup (b) Location of fracture initiation points

Fig. 2 The Configurations of fragmentation test

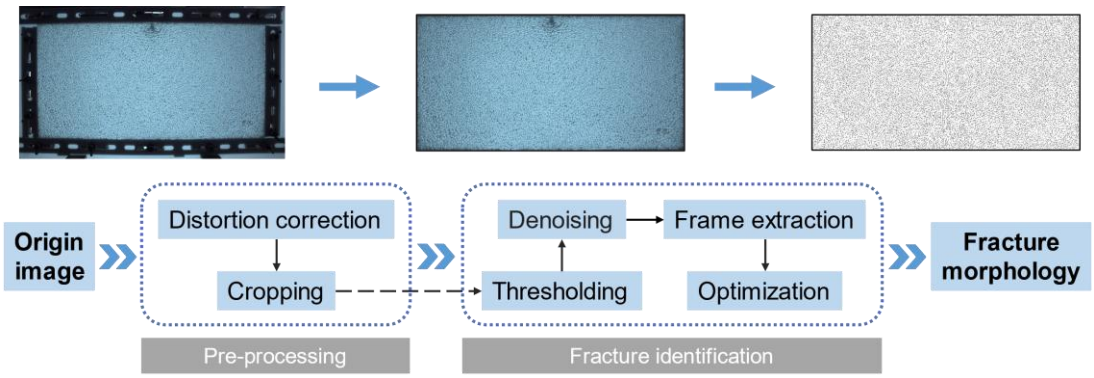

Fig. 3 Procedures of fracture morphology processing based on computer vision

Fig. 4 shows the fracture morphological image with the fracture initiation point in the centre. The local image with a size of 50 mm × 50 mm was used to highlight the difference. It can be seen that in the specimens having the same thickness, the fragment density significantly rises with the increase of surface compressive stress. Meanwhile, it could be noticed that a pair of butterfly-shaped fragments greatly larger than the surrounding can be found at the origin of cracking in most specimens (marked with red polygons in **Fig. 4**). The fragment size shows a decreasing trend from the cracking initiation point to the outside, and tends to be uniform away from the cracking point. Besides, fragments with large areas or strip shapes, which are common in low tempering level groups, do not appear in the groups with higher surface compressive stress.

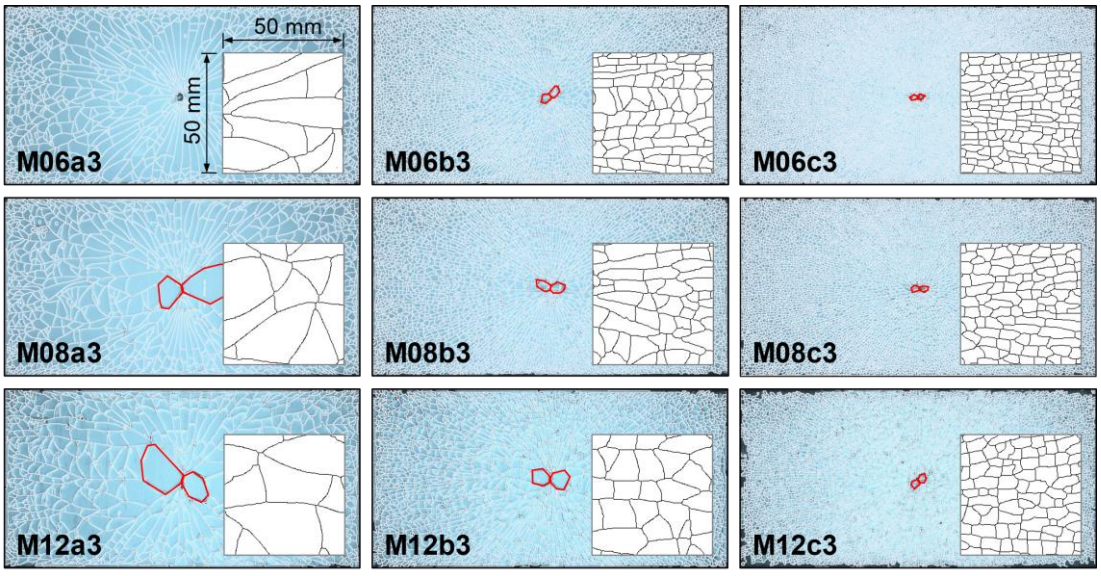

Fig. 4 Fracture morphology of selected heat-treated glass specimens

Considering that other characteristics are not intuitive, in addition to the fragment density,

statistical analysis on fragment shapes and their spatial distribution should be useful. It is assumed that the factors such as glass thickness, surface compressive stress and the location of fracture initiation can influence the propagation and formation of fracture morphology. The potential effects of these factors are subsequently discussed.

3. Results and discussion

In this section, a comprehensive analysis was performed to investigate the statistical and spatial features of fracture morphology from the extracted image groups. Crucial features including global and local density, fragment geometrical indexes and fragment centroids under the influence of several key factors (glass thickness, surface compressive stress, fracture initiation point) were analysed. The energy storage and release of glass were invoked to explain the findings.

3.1 Fragment density

3.1.1 Global fragment density

The representative fragment density of specimens is counted by global fragment density λ_G of the whole glass plane, which can be calculated by dividing the fragments number by the panel area. The statistical results are shown in **Table 3**. Linear regression equations were used to fit the global fragment density with the surface compressive stress. The equations and the corresponding coefficients of determination R^2 for each thickness of specimen are as below,

$$\text{6 mm:} \quad y = 0.169\,x - 12.122 \qquad (R^2 = 0.9997) \tag{1}$$

$$\text{8 mm:} \quad y = 0.104\,x - 6.582 \qquad (R^2 = 1.0000) \tag{2}$$

$$\text{12 mm:} \quad y = 0.074\,x - 3.923 \qquad (R^2 = 0.9999) \tag{3}$$

The data of the experimental results and the corresponding best-fit lines are given in **Fig. 5**, represented by solid markers and solid lines, respectively. The data points of the selected results from other reports [33, 34] are added with non-solid markers.

Table 3 Statistics of global fragment density λ_G (Unit: mm^{-2})

Thickness	Tempering level		
	Low	Medium	High
6 mm	8.05×10^{-3}	3.34×10^{-2}	5.28×10^{-2}
8 mm	6.40×10^{-3}	2.22×10^{-2}	4.19×10^{-2}
12 mm	5.57×10^{-3}	1.34×10^{-2}	3.03×10^{-2}

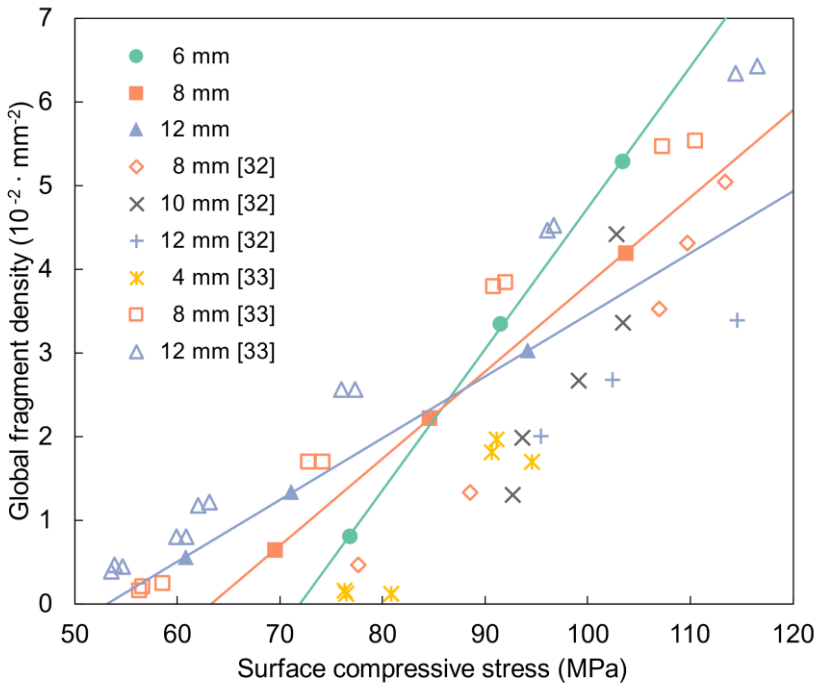

Fig. 5 Relationship between global fragment density and surface compressive stress

From Eqs. (1)-(3) and **Fig. 5**, it can be seen that for a given thickness, the global fragment density shows linear correlation to the surface compressive stress. Besides, although experimental data from different reports have slight variation in distribution, they basically follow the linear correlation as well.

The energy within the heat-treated glass is stored mainly as elastic strain energy. The stresses formed by tempering treatment are distributed parabolically along the thickness direction. The absolute value of surface compressive stress is nearly half of the mid-plane tensile stress [30, 35, 36]. The strain energy stored inside is hence mainly related to the tempering level and glass thickness. Heat-treated glass with higher surface compressive stress stores a higher level of strain energy, which indicates more stored energy will be released to generate more cracking surfaces and fragments in fracture process. Thus, it is rational that the fragment density increases with the growth of the surface compressive stress.

Comparing the results of glass specimens with different thicknesses, it can be seen that the curves intersect near the points around 86 MPa. The fragment density of 12 mm thick glass specimens is nearly three times higher than that of 8 mm thick ones, when the surface compressive stresses are 70 MPa. This phenomenon is due to that the thicker heat-treated glass could store larger amount of strain energy, which can be released during the fracture process.

However, the relationship between λ_G and σ_s presents a reverse trend when σ_s exceeds 86 MPa. In the glass specimens with higher tempering level, thicker glass obtains lower fragment density. This might be explained by the different proportions of strain energy which is released to generate the fragment surfaces at fracturing. Although more strain energy is stored in thicker heat-treated glass with the same tempering level, the energy proportion consumed to generate fragment surfaces is smaller, as the energy transferred or secondarily stored via other forms such as fragment expansion occupies a higher proportion at fracturing. Additionally, to generate same fracture morphology, thicker glass corresponds to a larger area of cross-section, implying a higher energy requirement. Statistics and analysis will be provided in detail in section 3.3.

3.1.2 Local fragment intensity

Local fragment intensity was adopted to describe the disparities of fragment number distributed at different areas of glass specimens. This is due to the various edge effects near fracture initiation points, which greatly affect the branching process of cracks and local morphology. The local fragment intensity of 12 mm thick glass specimens was selected and shown as the form of heatmap in **Fig. 6**. The fracture initiation points were marked with red crosses.

It can be seen that the fragment intensity at the fracture initiation point is lower than that from the adjacent areas. This shows the suppression of the cracking near the initiation point. Similar observations were also found in the experiments by Tandon et al [37], which reported that the fragment size decreased with the distance away from the fracture initiation. Besides, when the fracture initiation point is at the symmetric line of the glass specimens (*i.e.*, fracture points 2 and 3), the local fragment intensity presents an evident symmetrical feature (**Fig. 6** (b) and (c)). The local intensity also presents a trend of propagating outward from the fracture initiation point in a manner characterized by the alternations of peak and trough. Due to the limitation of specimen size, only one cycle of local intensity variation is achieved in most tests, whilst in specimens fractured at the corner (*e.g.*, **Fig. 6** (a)), two cycles of local intensity variation can be roughly observed along the diagonal path. The rough locations of the cycles are marked by white dotted lines in the figures.

However, this phenomenon seems to be interrupted in several regions due to complicated factors such as the vibration caused by the cracking load and fracture process, the stress waves and their reflection at the fixed boundary [38, 39], as well as the interaction between cracks and self-

emitted acoustic waves [40].

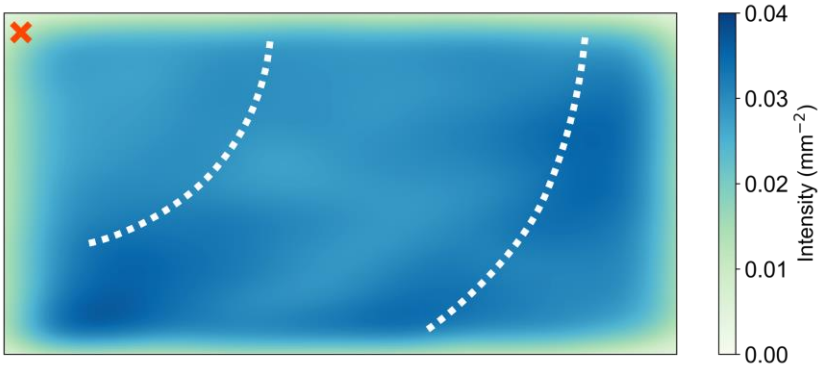

(a) M12c1 (12 mm, high tempered, fracture initiation point 1)

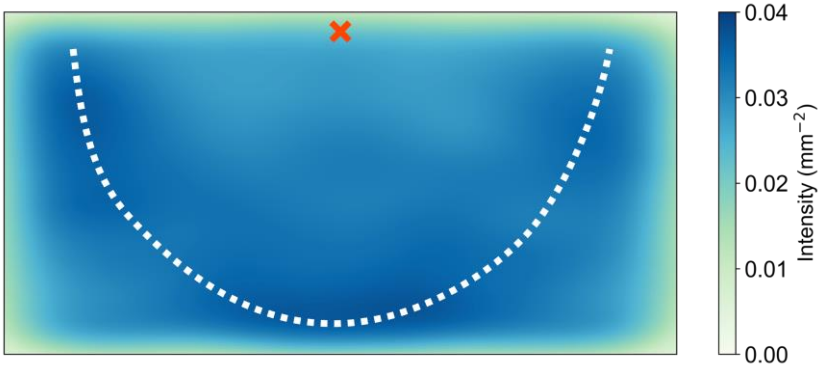

(b) M12c2 (12 mm, high tempered, fracture initiation point 2)

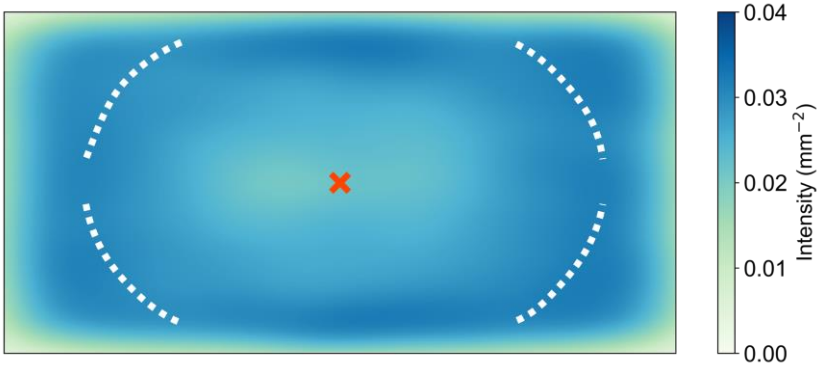

(c) M12c3 (12 mm, high tempered, fracture initiation point 3)

Fig. 6 Fragments intensity heatmaps

The results also show that the local intensity at the glass edges is significantly higher, along the edges there are very dense fragments. Due to the limitation of the statistical approach, the intensity heatmap does not accurately reflect the intensity situation near the edges. However, it can be visualized by the actual images of fracture morphology that the fragment intensity at the edges increases significantly. The shape of the fragments also differs from those in the inner region, being relatively more elongated. This may be caused by the complex stress distribution at the edges of the heat-treated glass, due to the edge polishing and the tempering process.

3.2 Geometrical statistics

The fracture morphology of the heat-treated glass panel is represented by many small fragments. **Fig. 7** shows typical fragments with significantly different shapes in two dimensions (2D) (sharper fragment and blunt fragment). The shape features of the fragments can greatly differ even with similar fragment areas, which depends on the tempering level and the locations of fragments.

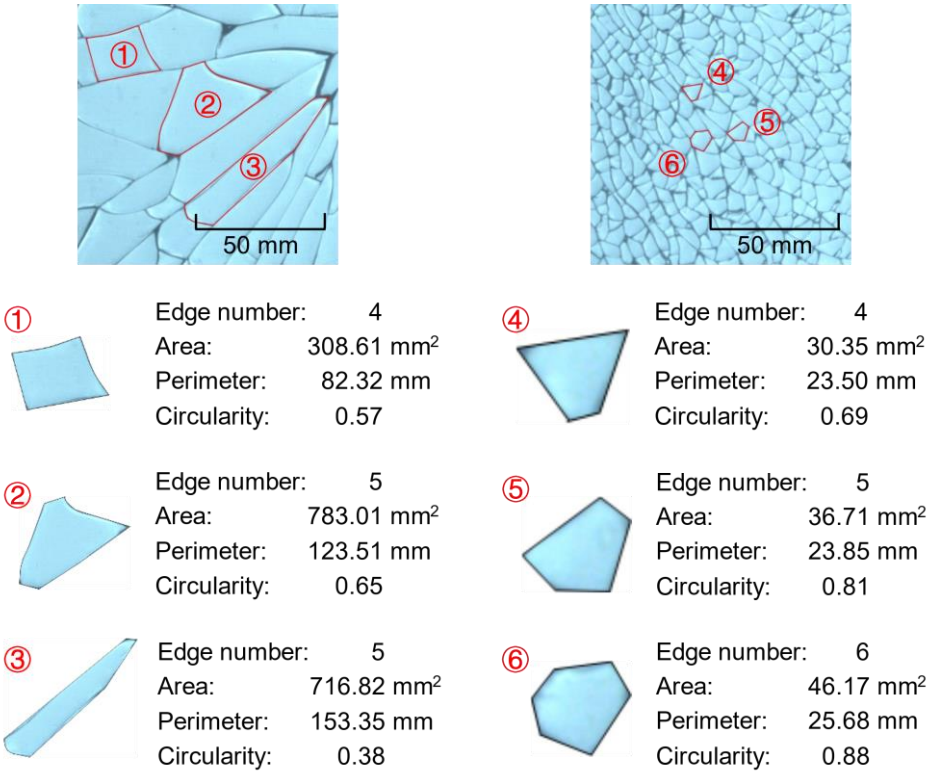

Fig. 7 Fragments with different shapes

The fragments can be approximated as prisms with the same thickness, and the value of thickness can be temporarily omitted. In 2D plane, the fragment can be simplified as a polygon and the number of edges is one of its basic geometrical features. Although most cracks in actual fracture morphology are not straight lines, making it difficult to do a straightforward count on the number of fragment edges. A simplified statistical approach was adopted. The common edges of neighbouring regions are considered as straight-line segments (it can be approximated by this way in most cases), the edge number of each fragment polygon can then be determined by counting the number of its neighbouring fragments. A simple example is shown in **Fig. 8**, the pentagon has five neighbouring regions, corresponding to its five edges (marked with green double vertical bars,

disregard the adjacency at the vertexes only).

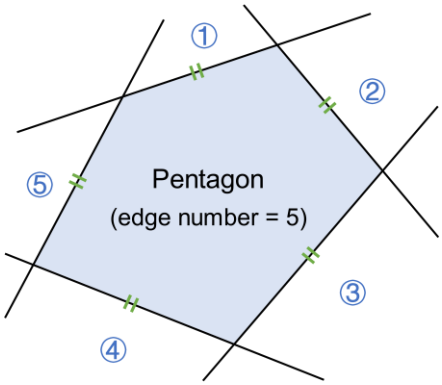

Fig. 8 Simplified statistical treatment on the number of fragment edges

Statistics show that the edge number of all fragments generated in the fragmentation tests has an average value close to 6 (5.92). The percentages of fragments with various edge numbers are shown by donut chart in **Fig. 9**. It can be seen that the edge number of the fragments ranges mainly from 4 to 7, which accounts for nearly 90%. Amongst the fragment shapes, hexagons have the highest percentage at over 30%, and pentagons share 26.8%. These two shapes have a percentage over 50% of the total number and act as the predominant shapes.

Further statistics indicate that the number of hexagonal fragments is the highest in most cases, with 59 out of 81 specimens. In the remaining specimens, 21 specimens have more fragments with five edges than other edge number, except for one group that generates more quadrilateral fragments. It is noted that these remaining specimens are mainly with relatively low tempering level. It might be due to the presence of large isolated fragments that promotes the generation of more fragments with low edge number. Moreover, although the hexagonal fragments are not predominant in these cases, their number is highly close to that of pentagonal fragments and thus to present great significance. This can also be supported by the previous calculation on the average edge number of the fragments. In **Fig. 10**, the percentage of fragments with various edge numbers is counted in groups according to the thickness and tempering level. Apparently, for the specimens with the same thickness, the percentage of pentagons and hexagons increases significantly with the rise of surface compressive stress. For the groups with lower tempering level, the combined percentage of pentagonal and hexagonal fragments is less than 50%, which can increase to around 60% with higher

surface compressive stress. Thus, the percentage of fragments with other edge numbers is relatively compressed.

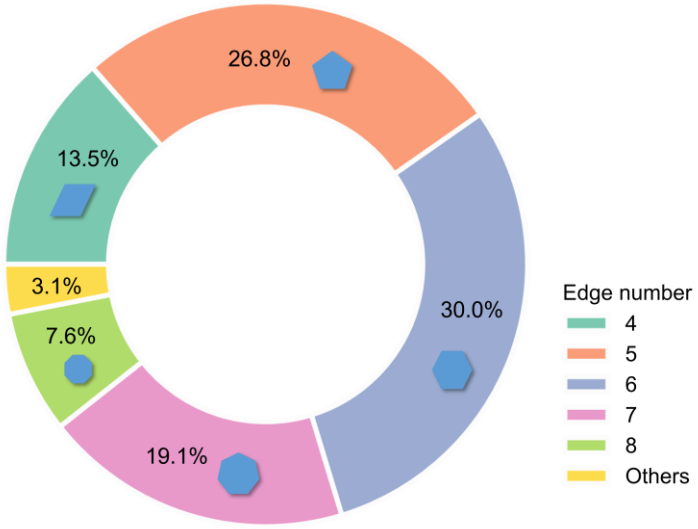

Fig. 9 Percentages of fragments with various edge numbers

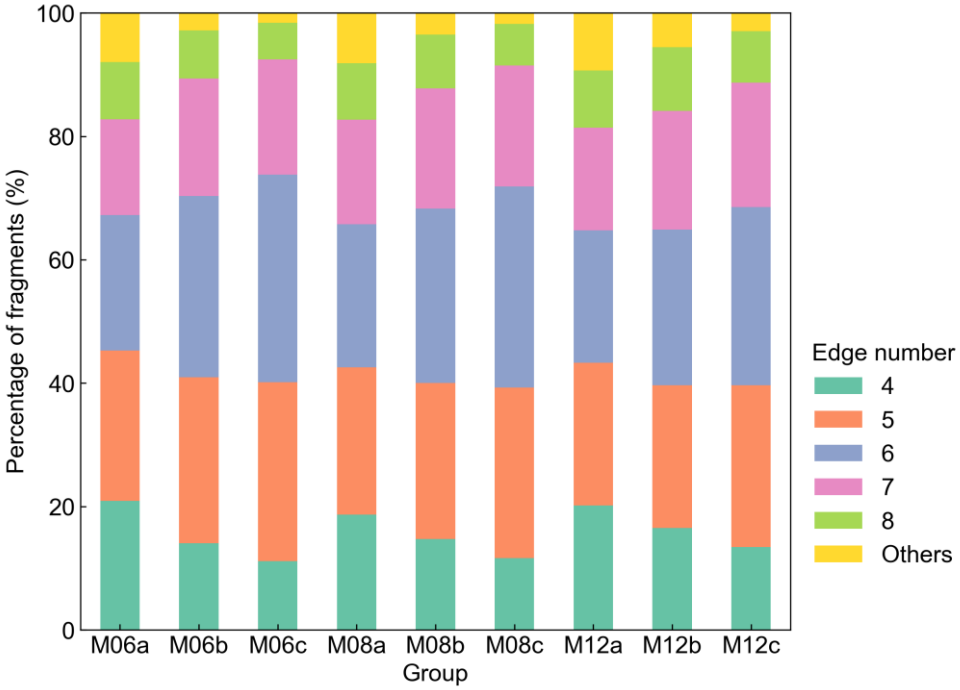

Fig. 10 Grouping statistics for the percentage of fragments with various edge numbers

Measured by size data, the geometrical features of fragments can be characterized by basic indexes such as area *S* and perimeter *C*. In order to describe the difference of shape features,

circularity φ is also introduced. Circularity denotes the roundness of a fragment and its quality being in the shape of circle, which can be calculated as:

$$\varphi = (4\pi S) / C^2 \quad (4)$$

For a fragment with a shape close to a positive circle, the circularity approaches 1, and vice versa the circularity is close to 0.

The correlation between fragment size and shape can be found. **Fig. 11** (a) shows the bivariate graph based on the data of area and circularity from group M12a. From the marginal histograms of the probability density (PD), it can be seen that the fragment sizes concentrate within an interval close to 100 mm^2, with the values of circularity around 0.65. The upward trend in the upper left corner (see the blue arrow) shows that the smaller fragment is more likely to have a circularity relatively higher. Additionally, the bivariate graphs of group M12b and M12c (specimens of the same thickness with different tempering levels) are plotted in **Fig. 11** (b) and (c), respectively. It can be seen that the graphs present similar distribution and tendency to that from **Fig. 11** (a). The only difference is the reduction and the leftward shift of the concentration interval of area, which is related to the growth of the tempering level.

According to the observation in section 3.1, the location of fracture initiation shows influences on the spatial distribution of fragments, leading to different trends of fragments size and shape likely to form in each region. However, its effect on the overall tendency of fragment size cannot be identified directly from the image. The scatter plot of area-perimeter and their probability statistics are then shown in **Fig. 12** to find the corresponding effect. The data of different fracture initiation points is marked with different markers, and the graphs are grouped by specimens' thickness and tempering level. Take the statistic of group M06c (**Fig. 12** (c)) as an example, most of the data points are located in a limited range, which corresponds to the fragment area less than 70 mm^2 and perimeter less than 55 mm. The data points outside this range are highly sparse, regardless of the fracture initiation of glass specimens. Other graphs have similar characteristics, except that the size distribution of the fragments varies between groups. It is seen that in specimens with the same thickness and tempering level, there is no significant difference in the PDs distribution of the fragment geometry parameters with different fracture initiations. Thus, the location of fracture initiation can be considered to have a very limited effect on the favourable distribution range of the fragment size.

1

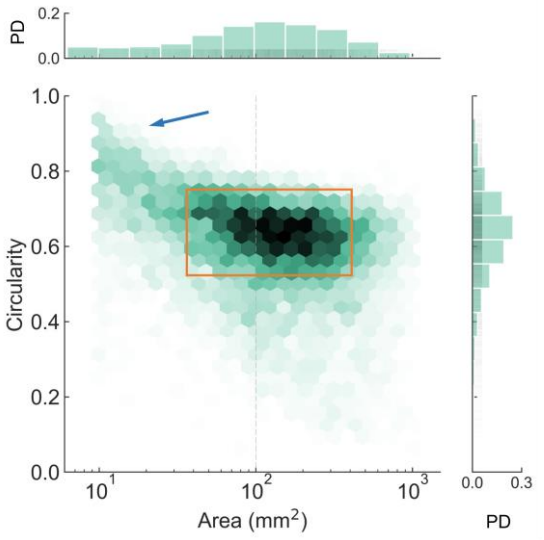

(a) M12a

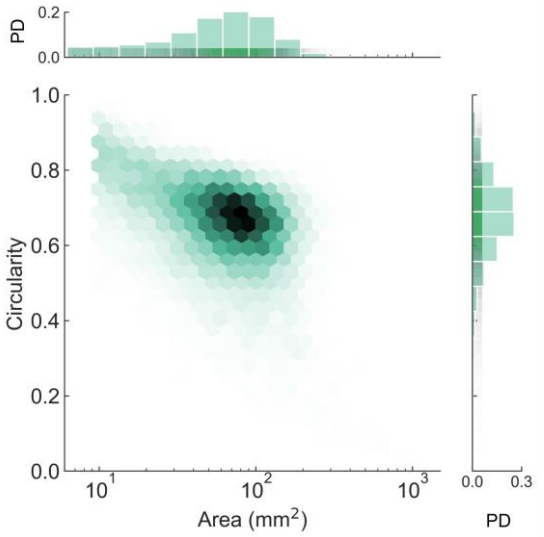

(b) M12b

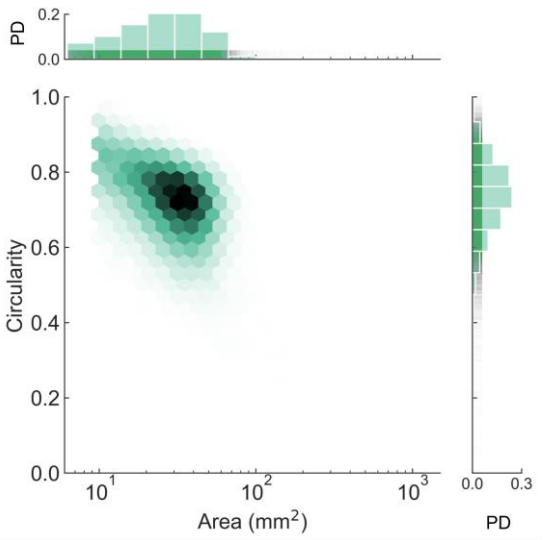

(c) M12c

2 **Fig. 11** Bivariate analysis about area and circularity

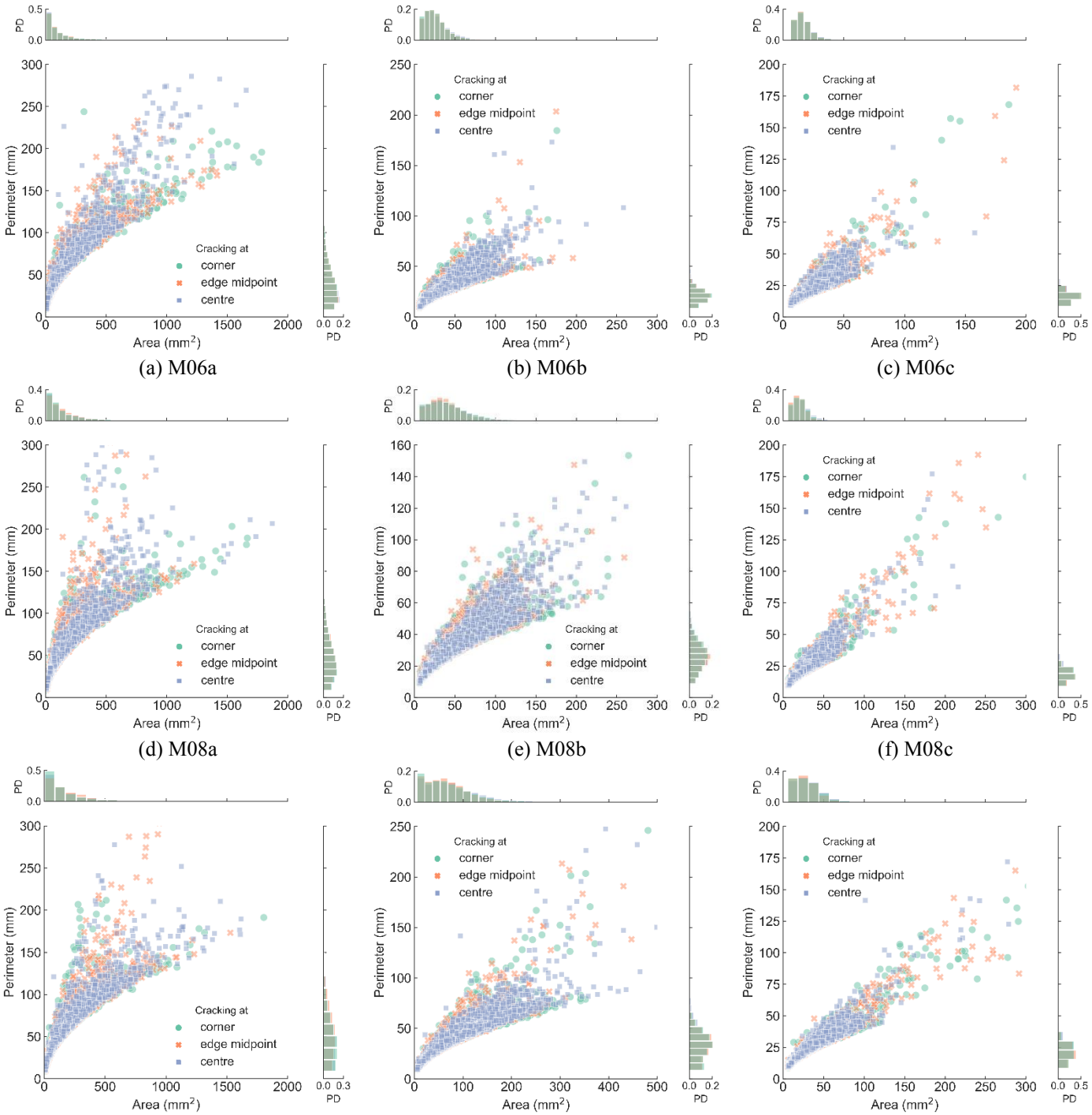

(a) M06a (b) M06b (c) M06c

(d) M08a (e) M08b (f) M08c

(g) M12a (h) M12b (i) M12c

Fig. 12 Effect of cracking initiation location on the fragment geometry

It is obvious that the tempering level has significant influences on the distribution of fragment size. For specimens with different levels of surface compressive stress, the fragment geometry parameters are counted in the groups of thickness, and the graphs of their PDs are plotted in **Fig. 13**. From **Fig. 13** (a) and (b), it can be seen that with the rising of tempering level, the size of fragments shows a decreasing trend. Take specimens with a thickness of 6 mm as an example, the

peak PD of fragment area decreases from 62.51 mm^2 to 16.61 mm^2, and the perimeter decreases from 41.20 mm to 16.86 mm, which indicates the number of fragments generated within the same area increases correspondingly.

Besides, the reduction in the range of values of the fragment size should be noticed, which indicates a reduction in the dispersion of the fragment size, implying a more uniform shape of the fragments for glass with a higher tempering level. Meanwhile, the fragment circularity gradually increases. Its peak value increases from 0.65 to around 0.75 with the growth of the tempering level, which shows the fragments' shape tending to be circular as the size decreases. In addition, it is noted that the smaller fragment size tends to present a higher circularity value.

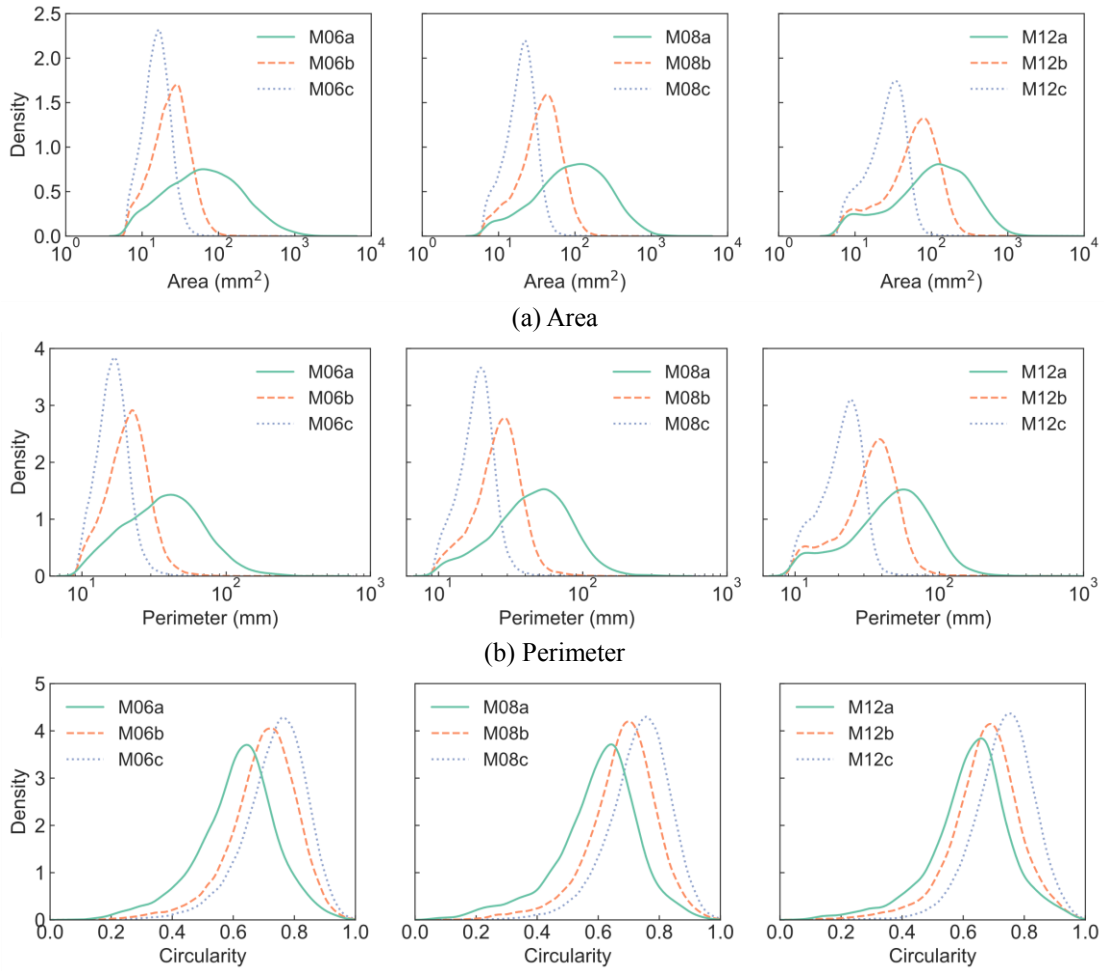

(a) Area

(b) Perimeter

(c) Circularity

Fig. 13 Effect of surface compressive stress on the fragment geometry

Table 4 The peak probability density values of the fragments' geometry parameters

Group	6 mm			8 mm			12 mm		
	M06a	M06b	M06c	M08a	M08b	M08c	M12a	M12b	M12c
Area (mm^2)	62.51	28.51	16.61	120.41	43.22	22.04	127.18	80.46	33.83
Perimeter (mm)	41.20	22.14	16.86	53.71	29.06	19.67	55.97	38.53	24.46
Circularity	0.652	0.731	0.766	0.650	0.704	0.766	0.657	0.691	0.755

3.3 Total crack length, fracture section and surface energy

Fractured glass can be considered as the assembly of fragments. From another aspect, fractured glass is generated by the crack branching within intact glass. In a two-dimensional plane, the fracture morphology is featured as many interrelated lines, and the total crack length L_C can be determined from the fragment perimeters, that is

$$L_C=\frac{1}{2}\sum C_i - C_S \tag{5}$$

where C_S represents the total edge length of the glass specimen, C_i is the length of each crack.

Combined with the glass thickness t, the crack corresponds to the fracture surface in three dimensions (3D). The cross-sectional area of fracture surface S_C can be roughly estimated as

$$S_C = 2tL_C \tag{6}$$

In this case, each segment of the crack corresponds to two surfaces.

Based on the data of fragments' perimeter, total crack length and cross-sectional area of fracture surface are calculated. **Fig. 14** shows the results with corresponding surface compressive stress. It can be seen that the specimens with the same thickness and tempering level have similar crack lengths, regardless of the fracture initiation point.

In the specimens with the same thickness, the total length as well as the cross-sectional area of cracks increase with the growth of surface compressive stress as expected. However, for the specimens with similar surface compressive stress, it should be noticed that the total crack length was not necessarily longer or shorter as the thickness increased, while the thicker glasses always correspond to a higher cross-sectional area of cracks. Take groups M08a (8 mm thick) and M12b (12 mm thick) as examples, in which the specimens have close surface compressive stresses of around 70 MPa. Both the crack length and the cross-sectional area of the thicker specimen are significantly larger than that of the thinner one (41.61 m to 29.41 m and 0.50 m^2 to 0.24 m^2). Considering the specimens in groups M06c (6 mm thick) and M08c (8 mm thick), which have nearly

the same surface compressive stresses (around 103 MPa). It can be found that the total crack length of the thicker glass (71.27 m) is shorter than the other one (79.50 m), which is opposite to the previous example. Nevertheless, the cross-sectional area of thicker glass (0.57 m^2 on average) is still higher than the thinner one (0.48 m^2 on average). Considering that glass fracture is the result of interfacial separation, it is more reasonable in a physical sense to compare the fracture cross-sectional area that considers the thickness.

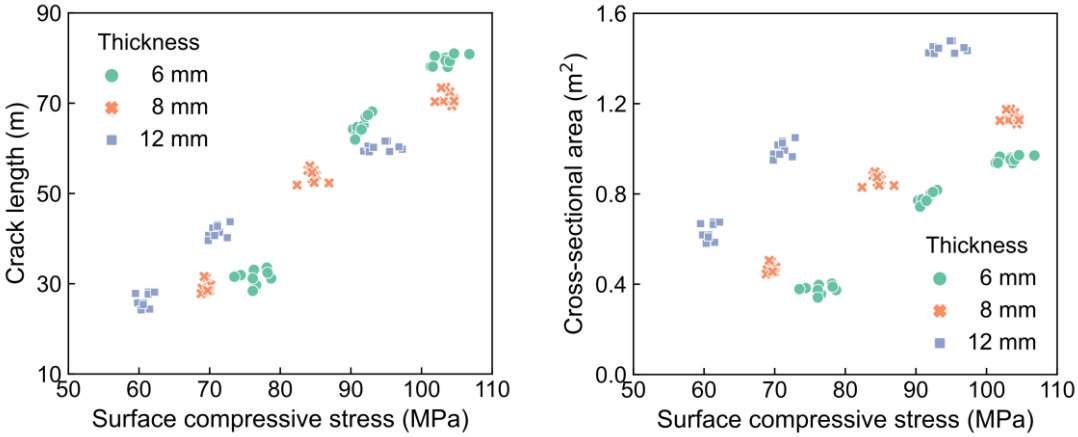

(a) Total crack length (b) Cross-sectional area of fracture surface

Fig. 14 Crack length (2D) and cross-sectional area (3D) of fractures with corresponding surface compressive stress

The fracture process of heat-treated glass is related to the release of strain energy stored in the glass [30, 41]. Most of the released energy is dissipated to generate crack surfaces (crack length in 2D) or transformed into the kinetic energy of the crack front [42, 43]. Thus, the total length of cracks is highly related to the energy released at fracture. Assumed γ_0 as the energy required to propagate crack per unit (also called fracture surface energy). Thus, for the specimens with a total fracture cross-sectional area of S_C, the energy E_f to generate the fracture morphology should be

$$E_f = \gamma_0 S_C = 2\gamma_0 L_C t \tag{7}$$

According to the findings in Refs [44, 45], the fracture surface energy E_f can be affected by various factors including glass composition leading to different elastic modulus, temperature, etc. At room temperature, the fracture surface energy ranges from 3.50 to 11 J/m^2 based on experiment results. Besides, through the bond breakage involved in the fracture process [46, 47], the theoretical value of fracture surface energy E_f was derived as 0.62 - 4.99 J/m^2 [48]. However, determining fracture surface energy is not the main concern of this study. The glass specimens used in the

fragmentation tests were made of the same raw material and the test was conducted in a controlled environment, which indicates the specimens were expected to have the same fracture surface energy. Therefore, γ_0 can be considered as a constant in the analysis and be reserved in the calculations.

As the surface compressive stress of heat-treated glass has been measured and collected, the strain energy stored inside the glass per unit cross-sectional area can be obtained as [22],

$$U_0=\frac{1\text{-}\nu}{5E}t\sigma_s^2 \tag{8}$$

where E represents the Young's modulus and ν represents the Poisson's ratio of glass, which keep constant in the study due to the use of the same glass material.

Through dividing the energy U_0 by the fracture surface energy, the ratio of the energy transferred to generate the fracture morphology can be estimated as

$$\frac{E_f}{U_0}=\frac{10\gamma_0 E}{1\text{-}\nu}\cdot\frac{L_C}{\sigma_s^2} \tag{9}$$

where the parameters γ_0, E and ν are constants related to the material properties. The ratio only depends on the value of L_C / σ_s^2, which is defined as the coefficient ψ of the fracture energy ratio.

In **Fig. 15**, the correlation between ψ and surface compressive stress is plotted. Due to the limited number of available data (three data points for each group of thickness), the fitting of the data points is not able to determine the exact value. However, the trend of the coefficient can still be estimated. The coefficient of each group increases first and then decreases with the rising of surface compressive stress. This indicates that the ratio of strain energy transferred to generate the fractures is not constant, and will vary with the strain energy storage.

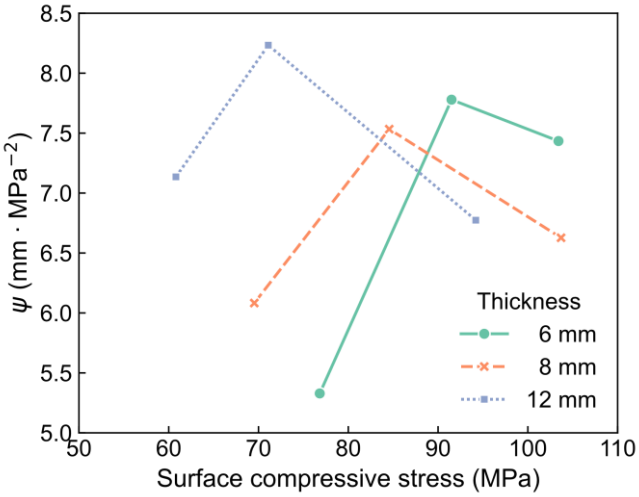

Fig. 15 The variation of the coefficient ψ with surface compressive stress

It is assumed that the release of strain energy is affected by the energy storage and the mechanism of fracture generation. The crack propagation in glass requires the release of potential energy exceeding the fracture surface energy of two new surfaces (each crack has two sides). In the case with lower surface compressive stress, the strain energy stored is relatively lower, indicating a lower energy density inside glass. Thus, difficulties rise to release enough energy for propagating cracks in most areas, which limits the length of the cracks. The energy is remained inside glass due to the reversible deformation before fracture. With the increase of surface compressive stress (which refers to a higher energy density), the energy released is easier to achieve the threshold and to further generate cracks. Thus, the release rate of strain energy increases, which results in the growth of the fragment density. However, the increase of strain energy does not consistently correlate positively to crack generation. Once the density of strain energy reaches a certain value, the fragment size becomes more difficult to decrease despite that there is available energy to promote the fracture process. Influenced by the factors such as size effect and edge effect, the further increase of fragment density requires higher fracture surface energy per unit to trigger. As a result, the variations in **Fig. 15** show that the coefficient ψ tends to increase at first and then decrease with increasing the surface compressive stress.

It is observed that the curves move left with thicker specimens, which capture the peak value at a lower surface compressive stress. This is due to that the thicker glass stores more strain energy per unit area with the same surface compressive stress. The thicker glass will limit the generation of larger fragments. Thus, the higher strain energy cannot be more efficiently released.

3.4 Spatial features of fragment centroids

Distance-based statistical method was introduced for the spatial analysis of fragment centroids patterns. The distribution of planar points can be reflected by the distance between each point and its nearest neighbour point, *i.e.*, nearest neighbour distance η. The nearest neighbour distance can be used to analyse the distribution of fragment centroids, which can promote and evaluate the reconstruction of fracture morphology.

For the point set with a determined global fragment density λ_G, the minimum nearest neighbour distance η_{min} shows its distribution trend. When the distribution of points is completely uniform,

η_{min} reaches the maximin value

$$d_0 = \sqrt{\frac{2}{\sqrt{3}} \cdot \frac{1}{\lambda_G}} \tag{10}$$

The value of η_{min} approaches towards d_0 in a dispersion situation, whilst the η_{min} will decrease until zero if the points are clustered. Based on this characteristic, the uniform parameter α was introduced to identify the distribution tendency of the point set, which is calculated as

$$\alpha = \eta_{min} / d_0 \tag{11}$$

The value of α is in the range of [0, 1]. The point pattern shows clustering when α reaches 0, whilst it shows dispersion when α is close to 1.

Take group M08b as an example, the maximum, minimum and average values of nearest neighbour distance are listed in **Table 5**. The result finds a small standard deviation which indicates the fracture initiation location has very limited influence on the nearest neighbour distance.

Table 5 Centroids distribution parameters with different fracture initiation points of group M08b

Group	η_{min} (mm)	η_{max} (mm)	η_{avg} (mm)	α
M08b1	2.42	9.20	5.20	0.33
M08b2	2.58	8.93	5.00	0.37
M08b3	2.59	9.41	5.13	0.35
Avg.	2.53	9.18	5.11	0.35
Std.	0.078	0.199	0.081	0.014

Therefore, it can be simplified in the parameter statistics of centroids distribution by ignoring the factor of the fracture initiation location. In **Table 6**, the parameters of fragment centroids distribution are collected according to the specimen thickness and tempering level. It is noted that the nearest neighbour distance shows an overall decreasing trend with the increase of the tempering level in the case of determined thickness, which is also a reflection of the increasing density of fragment centroids. In particular for η_{min}, its value is found to be roughly linearly correlated with the surface compressive stress, as shown in **Fig. 16**. The fitted linear regression equations are as follows,

$$\text{6 mm:} \quad y = -0.018\,x + 3.866 \qquad (R^2 = 0.9974) \tag{12}$$

$$\text{8 mm:} \quad y = -0.020\,x + 4.294 \qquad (R^2 = 0.9861) \tag{13}$$

$$\text{12 mm:} \quad y = -0.018\,x + 3.990 \qquad (R^2 = 0.9420) \tag{14}$$

According to the value of R^2, the equations are well-fitted to the experimental observations. Besides,

the corresponding value of d_0 and α are also given in **Table 6**. It can be seen that α increases from nearly 0.2 to 0.4, showing that the degree of uniformity grows with the rise of the tempering level.

Table 6 Parameter statistics of fragment centroids distribution

Group	η_{min} (mm)	η_{max} (mm)	η_{avg} (mm)	d_0 (mm)	α
M06a	2.51	19.86	7.34	12.01	0.21
M06b	2.23	7.64	4.23	5.89	0.38
M06c	2.04	5.75	3.46	4.68	0.44
M08a	2.91	19.20	8.45	13.46	0.22
M08b	2.53	9.18	5.11	7.22	0.35
M08c	2.21	6.36	3.84	5.25	0.42
M12a	3.06	20.29	9.07	14.49	0.21
M12b	2.61	11.89	6.40	9.31	0.28
M12c	2.37	7.34	4.41	6.18	0.38

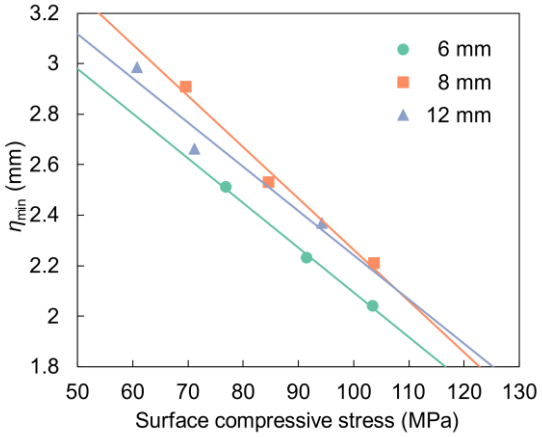

Fig. 16 Relationship between minimum nearest neighbour distance and surface compressive stress

4. Reconstruction of fracture morphology

In this section, a novel approach to stochastically construct the fracture morphology of heat-treated glass was proposed. The generation procedure can be classified into two steps. First, simulate the spatial distribution of feature points to locate the fragments. Second, the principle of Voronoi tessellation was introduced to partition the 2D plane according to the feature points and further determine the boundaries of fragments. The proposed method was evaluated to verify its effectiveness and applicability.

4.1 Simulation of feature points

Reconstructing the fracture morphology of heat-treated glass can facilitate the development of

a refined numerical model, which has more accurate local features of fractured glass. In most cases, it is sufficient to reproduce the fragments distribution at a global scale. The key step is to generate the point set (*i.e.*, a set of feature points) that can be used to determine the spatial positions of glass fragments.

Several potential methods can be used to simulate the points distribution including Poisson point process, Matérn hard-core point processes (MHCP) [49, 50] and Poisson disk sampling [51]. However, their outputs were found to be not satisfactory. According to the characteristics of fragment distribution, an enhanced and practical approach of point simulation was proposed in this study (**Fig. 17**). Global fragment density λ_G and minimum nearest neighbour distance η_{min} are considered as the key control parameters of the feature points simulation. Firstly, points should be evenly distributed on the plane based on a spacing of d_0 calculated by λ_G with Eq. (10). Afterward, movement along a random direction with a random distance is assigned separately to each point. The moveable range of each point is determined by η_{min} (can be obtained from the fragmentation tests data), which is a circle (*i.e.*, the purple circle in **Fig. 17**) with a radius of

$$r_c = (d_0 - \eta_{min}) / 2 \tag{15}$$

This random movement could also be considered as simulating a Poisson point process on the circle. The determined points are considered as the core points of the fragments. The theoretical value of the maximum nearest neighbour distance η_{max} can be deduced as

$$\eta_{max} = d_0 + r_c \tag{16}$$

according to the illustration in **Fig. 17**.

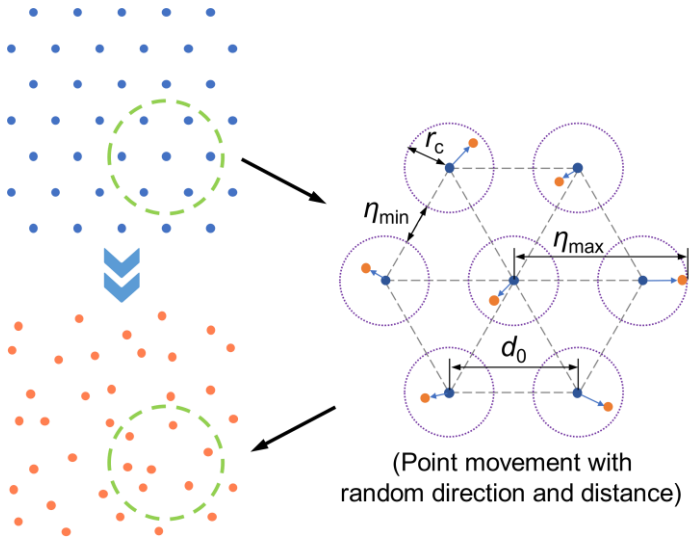

Fig. 17 Simulation of the feature points

It is a matter of concern for the acquisition of the two key control parameters, λ_G and η_{min}, in the point simulation approach. As mentioned in sections 3.1 and 3.4, it has been acknowledged that both λ_G and η_{min} have linear correlations with surface compressive stress σ_s, and the equations reflecting the correlations are acquired by the fragmentation tests (*i.e.*, Eqs. (1)-(3) and Eqs. (12)-(14)). Thus the values of λ_G and η_{min} can be obtained once σ_s is determined, as σ_s can be measured by non-destructive method with a surface stress meter in applications. It should be noted the equations might only be applicable to the glass of the same manufacturer. For glass from different sources, the equations are suggested to be reacquired.

The proposed method can effectively control the global fragment density and the point spacing. In **Table 7**, the experimental results from the fragmentation tests and the theoretical values calculated by Eq. (16) of η_{max} are compared. It can be seen that the deviations of most cases are within a small range. As for the only group with a deviation rate over 10%, M06a, a larger deviation is rational due to its more significant differences in fragment shapes at low tempering level.

Table 7 The comparison between experimental and theoretical values of η_{max}

Group	Experimental η_{max} (mm)	Theoretical η_{max} (mm)	Deviation value (mm)	Deviation rate (%)
M06a	19.86	16.75	3.11	18.57
M06b	7.64	7.72	0.08	1.04
M06c	5.75	6.00	0.25	4.17
M08a	19.20	18.74	0.46	2.45
M08b	9.18	9.56	0.38	3.97
M08c	6.36	6.77	0.41	6.06
M12a	20.29	20.20	0.09	0.45
M12b	11.89	12.66	0.77	6.08
M12c	7.34	8.08	0.74	9.16

To evaluate the point patterns from different simulation methods, experimental data of group M06b is taken to perform the comparative study, of which η_{min} is set as a fixed parameter. The spatial statistics toward simulation results are shown in **Table 8**. It can be seen that the results of MHCP and Poisson disk sampling have evident deviations from the experimental data, whereas the proposed approach presents higher overall accuracy of all examined parameters.

Table 8 Comparison of selected points distribution methods

Data	λ_G (mm^{-2})	η_{min} (mm)	η_{max} (mm)	α
Experimental data	3.34×10^{-2}	2.23	7.64	0.38
MHCP	2.42×10^{-2}	2.23	12.69	0.32
Poisson disk	11.75×10^{-2}	2.23	3.91	0.71
Proposed method	3.52×10^{-2}	2.29	7.62	0.40

The nearest neighbour distance distribution function, which is also commonly referred to as the *G* function [50], was subsequently introduced to quantitatively analyse and visualize the overall situation of the nearest neighbour distance η. *G* function is the cumulative distribution function (the integration of probability density function) of the nearest neighbour distance, indicating the rate less than the given distance *d* amongst the whole data, defined as

$$\mathrm{G}(d) = \sum_{i=1}^{n} \frac{\phi_i^d}{n} \tag{17}$$

$$\phi_i^d = \begin{cases} 1 & \text{if } \eta_i \le d \\ 0 & \text{otherwise} \end{cases} \tag{18}$$

where ϕ_i^d is an indicator function following Eq. (18) that judges if the nearest neighbour distance η_i of the randomly chosen point *i* is less than or equal to the value *d*.

The curves of *G* function can be used to evaluate the point pattern. Comparing the *G* function curves of simulated and experimental point patterns in **Fig. 18**, it can be seen that the curves are in good agreement.

In addition, *G* function can be used to identify whether the point pattern tends to be clustered or dispersed [52]. It has been acknowledged that *G* function has a theoretical expectation [49, 53] of

$$G(d) = 1 - \mathrm{e}^{\lambda\pi d^2} \tag{19}$$

while the underlying point process is a complete spatial randomness (CSR) process, which can be taken as the criterion to assess the trend of point distribution. For a given point process, it indicates that the point process is clustering if its *G* function plot is above the expectation, while the point process tends to be dispersed if the plot is below expectation. In this equation, λ is the intensity of the point process (mean point number per unit area). It can be seen in **Fig. 18** that the *G* function plots of simulated (solid curve) and experimental data (dashed curve) are both below the expectation curve of CSR (dotted curve), showing a dispersive trend of the point process.

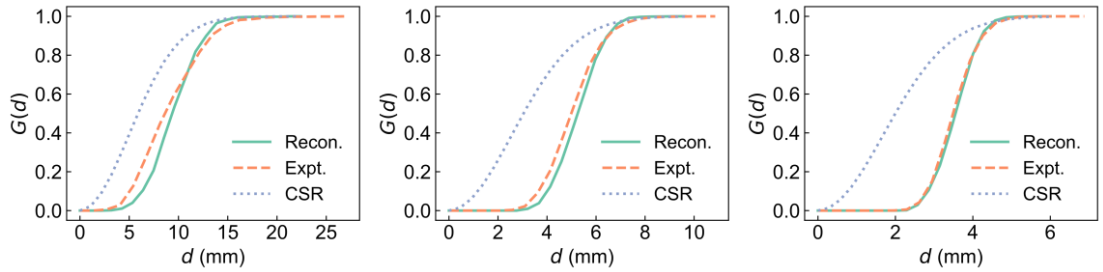

(a) M12a (12 mm, low tempered) (b) M08b (8 mm, medium tempered) (a) M06c (6 mm, high tempered)

Fig. 18 Comparison between reconstructed feature points and experimental data (based on *G* function)

The above work introduces the feature points distribution method, which achieves the first target to deploy points with identical density at a global scale, disregarding the influence of fracture initiation. It has been acknowledged that the location of fracture initiation has limited influence. Thus, in most cases for general analysis, fracture initiation does not need to be considered, and the basic scheme of feature point distribution is sufficient. Unless in the cases of fracture morphology reconstruction with higher accuracy requirements, the influence of fracture initiation might be involved. According to the discussion on local fragment intensity in section 3.1.2, the location of fracture initiation yields influences on the distribution of fragments. Therefore, the improvements of feature points simulation are performed by considering the fracture initiation location as the influencing factor. In the improvements, the local fragment intensity was introduced to finely control point distribution in each region, and the relationship between local fragment intensity and its distance from the fracture initiation points was considered for the controlling of the points simulation process.

It has been noticed from the heatmaps in **Fig. 6** that the variation of local fragment intensity is phased, depending on the distance to the fracture initiation, and is centrosymmetric. Thus, the glass plane can be partitioned into a series of concentric circles with the fracture initiation point as the centre, and the fragment distribution is examined separately to obtain the values of λ_G and η_{min} within each region. The principle of partition is to divide the continuous part with close intensity into the same region as far as possible. With the values of λ_G and η_{min}, feature points can be simulated within each region separately. The obtained distribution of feature points can reflect the local characteristics, which are influenced by the fracture initiation. In further consideration, the radius difference of the concentric circles could be minimized so the plane partition can be refined. This can be interpreted

as a differential form extension of the points simulation method at a global scale, and thus to satisfy the requirement for the distribution of fragment feature points considering the local reality.

Due to the local fragment intensity adopting the value based on the distance from the fracture initiation point, it is natural to introduce polar coordinates to determine the simulation parameters for the feature points deployment, and then transfer them into Cartesian coordinates. **Fig. 19** shows an example of feature points simulation in polar coordinates system, in which the local fragment intensity grows with the distance increases from the fracture initiation point. It should be noted that the left graph with blue dots shows the points being placed evenly considering local intensity, while the right graph with orange dots is obtained by the blue dots with random movement according to the restriction of $\eta_{\min}$. The red cross in the lower left corner represents the location of fracture initiation.

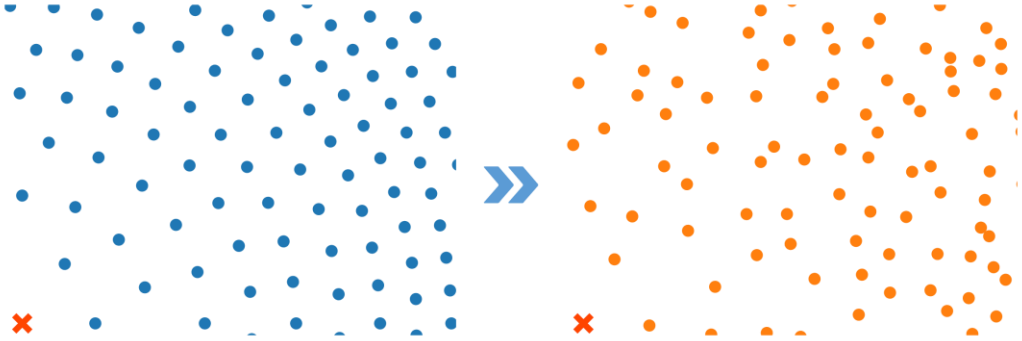

Fig. 19 Feature points simulation considering cracking initiation (partial as a demo)

4.2 Fragment boundaries determination by Voronoi tessellation

Following by confirming the locations of fragments by simulating the set of feature points, the 2D plane needs to be partitioned based on the determined feature points to define the intersected boundaries of the fragments.

Voronoi tessellation shows the potential to describe structures on micro and macro scales [31, 54]. As mentioned in references [28, 55, 56], Voronoi tessellation is likely to be suitable to describe the fracture pattern of bulk solid material with residual stress. Heat-treated glass with high surface compressive stress maps with such characteristics. Thus, Voronoi tessellation was employed in the fracture morphology reconstruction of heat-treated glass. The classic Voronoi tessellation in 2D provides a principle of partitioning the plane E into a series of convex polygons based on the given

set P of seed points $p_i \in P$. For each point p_i a Voronoi polygon R_i is generated as defined below [57, 58],

$$R_i = \{x \in E \mid d(x, p_i) \leqslant d(x, p_j) \text{ for all } j \neq i\} \tag{20}$$

where d denotes Euclidean distance. Each polygon R_i contains only one seed point p_i, making any location inside R_i closer to p_i than any other seed points in set P [59, 60]. Besides, hexagon is the most common polygon in Voronoi tessellation rather than polygons with other edge numbers [61], which coincides with the statistical findings on the edge number of fragments mentioned in section 3.2.

Based on a specimen from group M08b2, **Fig. 20** gives the comparison of actual and reconstructed fracture morphologies of three typical regions with different characteristics (marked as region 1, 2, and 3) to examine the applicability of the Voronoi tessellation. The actual fragments are denoted by blue irregular curves and the reconstructed fragment boundaries can be characterized by black lines. The solid dots are the centroids (also defined as the feature points, act as seed points in Voronoi tessellation) of the fragments. It can be seen that the Voronoi tessellation achieves well satisfaction to reproduce the fracture morphology after the feature points are determined. It is noted that the constructed morphology of regions with higher fragments circularity seems to be closer to the actual one than that with lower fragments circularity, *e.g.*, comparing region 1 and region 2 with region 3 in the given demo. This is beneficial when simulating the fracture morphology of fully tempered glass which has a high value of average fragment circularity.

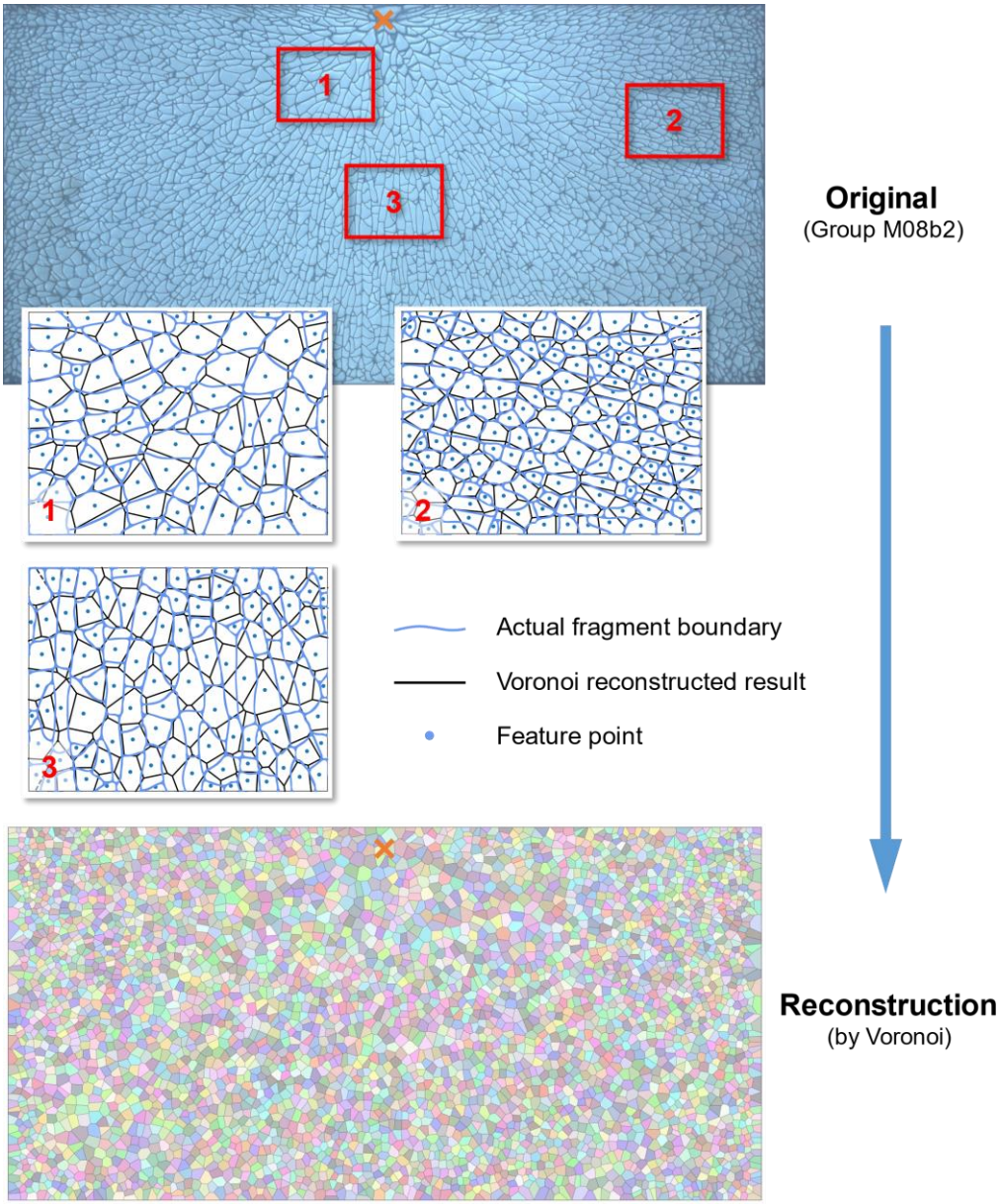

Fig. 20 The demonstration of Voronoi tessellation based on one specimen of group M08b2

PDs of the geometrical parameters from the reconstructed morphology were analysed and compared with those from the experimental data of a specimen from group M12c3 (**Fig. 21**). It is found that in the fracture morphology via Voronoi tessellation, the generated results can cover the major intervals of the geometrical parameters of fragments in the actual one. This comparison indicates that the reconstructed fragments by Voronoi concept can well simulate the actual situation. However, the generated results are also seen to present a narrower distribution band of the geometrical parameters, which suggests that the number of fragments having too large, small size or more irregular shapes from the simulated case is significantly lower than that from experimental

data. Differing from the finding that the value of geometrical parameters *S* and *C* at peak PD from the simulation is highly close to that from the experiment, the deviation of circularity is comparatively greater showing that the generated fragments are commonly more "blunt and circular" than the realistic ones. This might be caused by that the classic Voronoi tessellation partitions the plane with straight lines, whilst the actual morphology is more frequent to be with irregular curves. Furthermore, the plane partition principles of Voronoi tessellation require that any point in the divided polygonal area should be closer to the corresponding seed than any other seed in the remaining polygons, which results in the suppression of generating slender fragments with extreme sizes and small circularity. This can be found in **Fig. 20**, especially in the selected region 3 (multiple slender fragments can be found in this region).

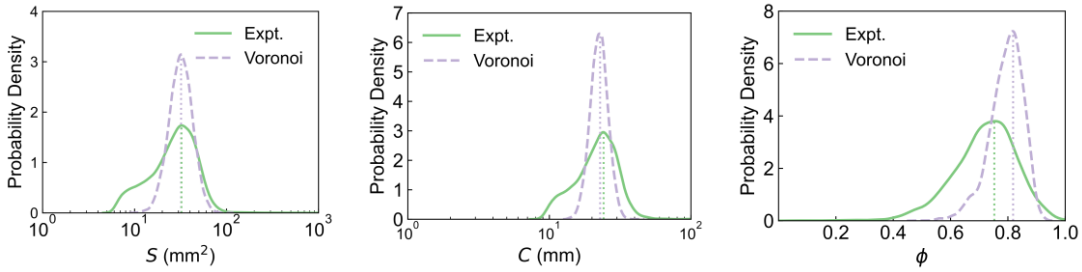

(a) Area (b) Perimeter (a) Circularity

Fig. 21 Comparison of Voronoi reconstructed morphology and experimental result

In summary, with the given location of actual fragments (defined by the feature points), it is appropriate to partition the glass plane and determine the boundaries of the fragments by the concept of Voronoi tessellation.

4.3 Output and evaluation of the reconstruction approach

Based on the works above, the complete approach of fracture morphology reconstruction can be concluded. The reconstruction procedures are as follows: 1) simulate and distribute the point set at the given plane as the feature points for the fragments, and then 2) partition the plane into elements following the principles of Voronoi tessellation, to create fragment boundaries. The output of the reconstruction approach is demonstrated and evaluated herein.

Based on the statistical data of group M06b (with the surface compressive stress of 91.50 MPa), an attempt to reconstruct the fracture morphology was carried out on a plane with the same size as the actual specimen. **Fig. 22** shows the reconstructed result, which shares a high similarity to the

fracture morphology of the reference glass. Further, the reconstructed results vary within a rational range due to the introduction of random parameters in the feature points deployment. This also coincides with the generation randomness of cracks in reality.

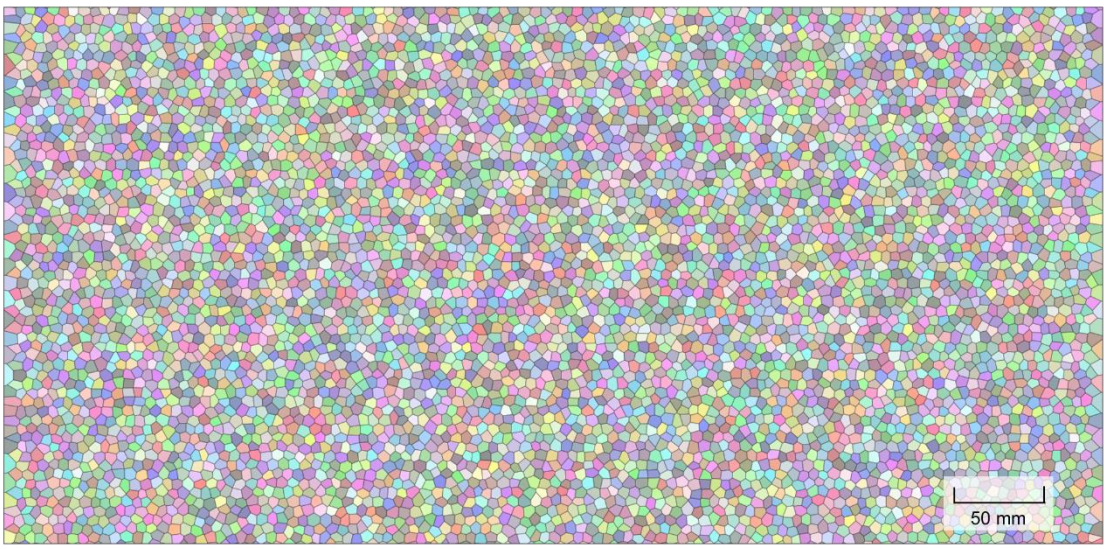

Fig. 22 Reconstruction output referring to group M06b without considering fracture initiation

For the purpose of evaluation, the fracture morphologies of all tested groups were reconstructed stochastically according to the statistical results obtained from fragmentation tests afterwards. **Table 9** gives the peak values of PDs from the reconstructed morphology and the experimental one. The standard deviation is commonly within 5%, which shows that the reconstruction results can well present the main features of the fracture morphology.

Table 9 Peak PDs of the reconstructed morphology and its comparison with experimental data

Group	Area (mm^2)		Perimeter (mm)		Circularity	
	Peak	Deviation	Peak	Deviation	Peak	Deviation
M06a	4.83	0.70	3.78	0.06	0.841	0.197
M06b	3.40	0.05	3.05	0.05	0.868	0.148
M06c	2.94	0.13	2.81	0.01	0.875	0.111
M08a	5.06	0.27	3.89	0.09	0.841	0.196
M08b	3.82	0.05	3.26	0.11	0.864	0.163
M08c	3.18	0.09	2.93	0.05	0.873	0.115
M12a	5.20	0.36	3.97	0.06	0.842	0.181
M12b	4.32	0.07	3.52	0.13	0.853	0.162
M12c	3.51	0.02	3.10	0.10	0.867	0.116

In addition, if the location of fracture initiation is determined, the feature points for the reconstruction process can be deployed considering its influence as mentioned in section 4.1. The reconstruction output is suitable to the situation with the requirement of high accuracy. However, it should be noted that the determination of the local intensity of feature points requires more testing data and further statistics. Herein, a reconstruction output demonstration of fracture morphology with a specified fracture initiation point (fractured at the lower left corner denoted by a cross marker) is shown in **Fig. 23**. The demo one has a size of 400 mm × 300 mm. The local intensity variation is considered in the simulation of feature points, based on the experimental data of group M12b. The reconstruction result reproduces the observation that the fragment intensity generally grows with increasing the distance from the fracture initiation point, showing the influence of fracture load on the fracture morphology of heat-treated glass.

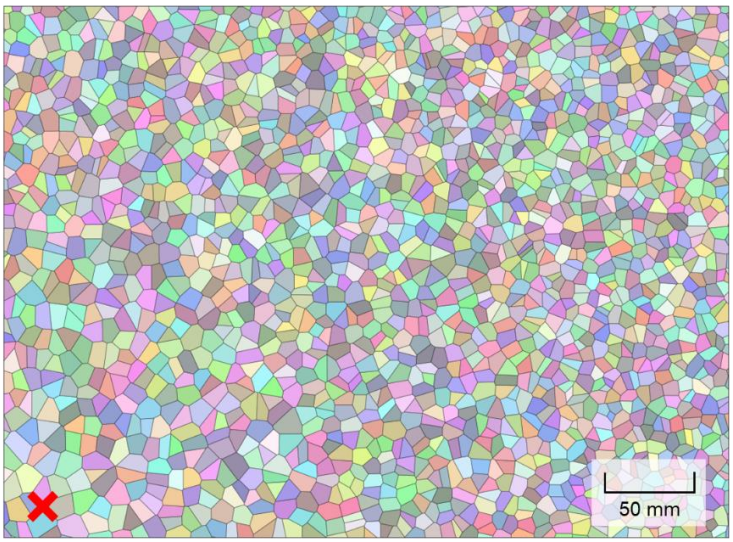

Fig. 23 Reconstruction output demo of fracture morphology considering fracture initiation

In general, the developed reconstruction process considering the global density and the neighbour distance of fragments is believed to be adequate for most application scenarios. It is unnecessary to over-consider the differences in the local distribution of fragments, which are mainly caused by the effect of the fracture initiation. Particularly, in the cases of large specimens, the influence of fracture initiation will be diminished. In such situations, it is only necessary to obtain the relationships of surface compressive stress with the parameters λ_G and η_{min}. The relevant data can be acquired from the pre-experiment or provided by the manufacturers. In real applications afterwards, the values of λ_G and η_{min} could be obtained with the non-destructive measurement of

surface compressive stress by surface stress meter, and the fragmentation tests (or other destructive tests) are no longer necessary. In certain cases, the reconstructed morphology might be over-uniformly distributed and the influence of the fracture initiation location should hence be considered if more precise analysis is demanded. For this purpose, detailed sub-regional data should be collected in pre-performed fragmentation tests to identify local distribution features of fragments, to provide support for the refined reconstruction of fracture morphology.

5. Concluding remarks

The information contained in the fracture morphology of glass is significant for understanding the post-fracture performances of structural glass, which is mainly composed by heat-treated glass. This study characterized the fracture morphology of heat-treated glass and proposed a novel method to reconstruct the morphology. Fragmentation tests of heat-treated glass with common-used thicknesses and a wide range of surface compressive stress are conducted, to investigate the morphological features and the corresponding influencing principles. A computer-vision-aided method towards transparent objects was developed for the identification of glass fracture morphology. Then the spatial distribution and geometrical features of fragment elements in fracture morphology, as well as the graphical patterns of fracture morphology, are collected and analysed in detail. The results indicate that the statistical and spatial features of fracture morphology on global scale are highly related to the inherent properties of heat-treated glass, but are less likely to be affected by external factors such as the location of fracture initiation, although the fracture pattern may still be locally affected by the fracture initiation load in a limited range. Correlations between typical parameters of fracture morphology and surface compressive stress were quantitatively presented to be linear. Meanwhile, the strain energy release in the fracture process is not constant for different types of specimens. A coefficient reflecting the energy release was introduced for assessment purposes. The release rate tends to increase and then decrease with growing surface compressive stress, and the glass thickness also limits the crack generation, which is approximately equivalent to the release of strain energy.

Based on the characterisation of fracture morphology, a novel reconstruction method was developed for describing the spatial and statistical features of fracture morphology. The method combined a new deployment approach of fragment feature points and the Voronoi tessellation

concept. In the reconstruction process, the inherent properties of glass and the local effects of the fracture load can be properly considered, and the control parameters are determined by data from fragmentation tests. The proposed method shows good satisfaction in reproducing fracture morphology, and its quantitative statistical indicators agree well with the experimental data. The deviation of selected indicators is less than 5%. This suggests that the characteristics of the fracture morphology of heat-treated glass can be well presented by the proposed method, which might contribute to the investigation into the post-fracture behaviour of structural glass components in future works via the following three aspects.

(1) Through the introduction of predefined fracture patterns stochastically generated by the reconstruction method, refined numerical models can be established, which meet the demand of more mechanical analysis while being less constrained by experimental conditions. Also, the refinement of the fracture morphology reconstruction can be further improved. Effects including the variety of surface compressive stress at different locations, edge effects as well as initial defects of glass are worth being considered. Nevertheless this means higher cost in characterization and a balance should be found between the accuracy of the reconstruction and its practical value.

(2) The images or data of fracture morphology can be combined with the artificial intelligence-based approach and the mechanical model to seek a smart, fast and physical based algorithm to estimate the stress-strain growth and the tearing inititian due to the local morpholgy of fractured structural glass components without running numerical models.

(3) The fracture morphology links to the strain energy release of glass and further the out-of-plane deformation of glass components due to the expansion of fractured glass. It can hence be used to give more accurate prediction on the local deformation after a large-size glass component fractures, which might trigger the buckling failure in certain cases.

Acknowledgement

This study was supported by the National Natural Science Foundation of China (grant numbers 51908352, 52078293) and the Science and Technology Innovation Plan of Shanghai Science and Technology Commission (grant number 20dz1201301).

References

[1] O'Regan C. Structural use of glass in buildings. 2nd edition. London: Institution Of Structural Engineers; 2014.

[2] Mauro JC, Zanotto ED. Two centuries of glass research: historical trends, current status, and grand challenges for the future. Int J Appl Glass Sci. 2014;5(3):313-27. https://doi.org/10.1111/ijag.12087.

[3] Guin J-P, Wiederhorn SM. Fracture of silicate glasses: Ductile or brittle? Phys Rev Lett. 2004;92(21):215502. https://doi.org/10.1103/PhysRevLett.92.215502.

[4] Wang X-e, Yang J, Liu Q-f, Zhang Y-m, Zhao C. A comparative study of numerical modelling techniques for the fracture of brittle materials with specific reference to glass. Eng Struct. 2017;152:493-505. https://doi.org/10.1016/j.engstruct.2017.08.050.

[5] Choi Y, Eon Lee S, Jung J-W, Hong J-W. Collision mechanism of unmanned aerial vehicles onto glass panels. Int J Micro Air Veh. 2021;13:17568293211060504. https://doi.org/10.1177/17568293211060504.

[6] Hidallana-Gamage HD, Thambiratnam DP, Perera NJ. Failure analysis of laminated glass panels subjected to blast loads. Eng Fail Anal. 2014;36:14-29. https://doi.org/10.1016/j.engfailanal.2013.09.018.

[7] Callewaert D, Belis J, Vandebroek M, Van Impe R. Spontaneous failure of a passable laminated glass floor element. Eng Fail Anal. 2011;18(7):1889-99. https://doi.org/10.1016/j.engfailanal.2011.07.010.

[8] Kasper A, Pyeonglae N, Yuan Z. Spontaneous cracking of thermally toughened safety glass Part two: nickel sulphide inclusions identified in annealed glass. Glass Struct Eng. 2019;4(3):315-43. https://doi.org/10.1007/s40940-018-00092-0.

[9] Pisano G, Bonati A, Royer Carfagni G. How the risk of failure in lifetime of tempered glass depends on the size of NiS inclusions and heat soak test duration. J Am Ceram Soc. 2021;104(1):383-403. https://doi.org/10.1111/jace.17413.

[10] Zhang X, Hao H, Ma G. Laboratory test and numerical simulation of laminated glass window vulnerability to debris impact. Int J Impact Eng. 2013;55:49-62. https://doi.org/10.1016/j.ijimpeng.2013.01.002.

[11] Pelfrene J, Kuntsche JK, Van Dam S, Van Paepegem W, Schneider J. Critical assessment of the post-breakage performance of blast loaded laminated glazing: experiments and simulations. Int J Impact Eng. 2016;88(88):61-71. https://doi.org/10.1016/j.ijimpeng.2015.09.008.

[12] Dharani LR, Ji F, Behr RA, Minor JE, Kremer PA. Breakage prediction of laminated glass using the “sacrificial ply” design concept. J Architect Eng. 2004;10(4):126-35. https://doi.org/10.1061/(ASCE)1076-0431(2004)10:4(126).

[13] Foraboschi P. Hybrid laminated-glass plate: Design and assessment. Compos Struct. 2013;106:250-63. https://doi.org/10.1016/j.compstruct.2013.05.041.

[14] Biolzi L, Orlando M, Piscitelli LR, Spinelli P. Static and dynamic response of progressively damaged ionoplast laminated glass beams. Compos Struct. 2016;157:337-47. https://doi.org/10.1016/j.compstruct.2016.09.004.

[15] Galuppi L, Royer-Carfagni G. The post-breakage response of laminated heat-treated glass under in plane and out of plane loading. Compos B Eng. 2018;147:227-39. https://doi.org/10.1016/j.compositesb.2018.04.005.

[16] Wang X-e, Yang J, Pan Z, Wang F, Meng Y, Zhu Y. Exploratory investigation into the post-fracture model of laminated tempered glass using combined Voronoi-FDEM approach. Int J Mech Sci. 2021;190:105989. https://doi.org/10.1016/j.ijmecsci.2020.105989.
[17] Bermbach T, Teich M, Gebbeken N. Experimental investigation of energy dissipation mechanisms in laminated safety glass for combined blast-temperature loading scenarios. Glass Struct Eng. 2016;1(1):331-50. https://doi.org/10.1007/s40940-016-0029-y.
[18] Wang X-e, Yang J, Chong WTA, Qiao P, Peng S, Huang X. Post-fracture performance of laminated glass panels under consecutive hard body impacts. Compos Struct. 2020;254:112777. https://doi.org/10.1016/j.compstruct.2020.112777.
[19] Zhao C, Yang J, Wang X, Azim I. Experimental investigation into the post-breakage performance of pre-cracked laminated glass plates. Constr Build Mater. 2019;224:996-1006. https://doi.org/10.1016/j.conbuildmat.2019.07.286.
[20] Nielsen JH, Olesen JF, Stang H. The Fracture Process of Tempered Soda-Lime-Silica Glass. Exp Mech. 2008;49(6):855-70. https://doi.org/10.1007/s11340-008-9200-y.
[21] Nielsen JH, Olesen JF, Stang H. Characterization of the residual stress state in commercially fully toughened glass. J Mater Civil Eng. 2010;22(2):179-85. https://doi.org/10.1061/(Asce)0899-1561(2010)22:2(179).
[22] Nielsen JH. Remaining stress-state and strain-energy in tempered glass fragments. Glass Struct Eng. 2017;2(1):45-56. https://doi.org/10.1007/s40940-016-0036-z.
[23] Nielsen JH, Bjarrum M. Deformations and strain energy in fragments of tempered glass: experimental and numerical investigation. Glass Struct Eng. 2017;2(2):133-46. https://doi.org/10.1007/s40940-017-0043-8.
[24] Bradt RC. The Fractography and Crack Patterns of Broken Glass. J Fail Anal Prev. 2011;11(2):79-96. https://doi.org/10.1007/s11668-011-9432-5.
[25] Tang Z, Abrams MB, Mauro JC, Zoeller LR, Venkataraman N, Hu G. High-speed camera study of Stage III crack propagation in chemically strengthened glass. Appl Phys A Mater Sci Process. 2014;116(2):471-7. https://doi.org/10.1007/s00339-014-8370-y.
[26] Lee H, Cho S, Yoon K, Lee J. Glass Thickness and Fragmentation Behavior in Stressed Glasses. New J Glass Ceram. 2012;02(04):116-21. https://doi.org/10.4236/njgc.2012.24020.
[27] Dugnani R, Zednik RJ, Verghese P. Analytical model of dynamic crack evolution in tempered and strengthened glass plates. Int J Fract. 2014;190(1-2):75-86. https://doi.org/10.1007/s10704-014-9975-z.
[28] Molnár G, Ferentzi M, Weltsch Z, Szebényi G, Borbás L, Bojtár I. Fragmentation of wedge loaded tempered structural glass. Glass Struct Eng. 2016;1(2):385-94. https://doi.org/10.1007/s40940-016-0010-9.
[29] Pourmoghaddam N, Kraus MA, Schneider J, Siebert G. The geometrical properties of random 2D Voronoi tesselations for the prediction of the tempered glass fracture pattern. ce/papers. 2018;2(5-6):325-39. https://doi.org/10.1002/cepa.934.
[30] Pourmoghaddam N, Kraus MA, Schneider J, Siebert G. Relationship between strain energy and fracture pattern morphology of thermally tempered glass for the prediction of the 2D macro-scale fragmentation of glass. Glass Struct Eng. 2018;4(2):257-75. https://doi.org/10.1007/s40940-018-00091-1.
[31] Wang X-e, Yang J, Huang X, Wang F, Zhu Y. Voronoi-FDEM concept for modelling post-fracture response of progressively damaged structural glass. Eng Comput. 2021:1-14.

https://doi.org/10.1007/s00366-021-01318-6.
[32] Bradski G. The OpenCV Library. Dr Dobb's Journal of Software Tools. 2000.
[33] Mognato E, Barbieri A, Schiavonato M, Pace M, del Vetro-Venezia S-SS. Thermally toughened safety glass: correlation between flexural strength, fragmentation and surface compressive stress. Glass Performance Days. 2011:115-8.
[34] Pourmoghaddam N, Schneider J. Experimental investigation into the fragment size of tempered glass. Glass Struct Eng. 2018;3(2):167-81. https://doi.org/10.1007/s40940-018-0062-0.
[35] Mognato E, Brocca S, Barbieri A. Thermally processed glass: correlation between surface compression, mechanical and fragmentation test. Glass Performance Days. 2017;2017:8-11.
[36] Zaccaria M, Overend M. Nondestructive safety evaluation of thermally tempered glass. J Mater Civil Eng. 2020;32(4):04020043. https://doi.org/10.1061/(Asce)Mt.1943-5533.0003086.
[37] Tandon R, Glass SJ. Fracture initiation and fragmentation in chemically tempered glass. J Eur Ceram Soc. 2015;35(1):285-95. https://doi.org/10.1016/j.jeurceramsoc.2014.07.031.
[38] Ha YD, Bobaru F. Characteristics of dynamic brittle fracture captured with peridynamics. Eng Fract Mech. 2011;78(6):1156-68. https://doi.org/10.1016/j.engfracmech.2010.11.020.
[39] Hu W, Wang Y, Yu J, Yen C-F, Bobaru F. Impact damage on a thin glass plate with a thin polycarbonate backing. Int J Impact Eng. 2013;62:152-65. https://doi.org/10.1016/j.ijimpeng.2013.07.001.
[40] Massy D, Mazen F, Landru D, Mohamed NB, Tardif S, Reinhardt A, et al. Crack front interaction with self-emitted acoustic waves. Phys Rev Lett. 2018;121(19):195501. https://doi.org/10.1103/PhysRevLett.121.195501.
[41] Bos F, editor Elastic strain energy release at failure and its consequence for structural glass testing and design. Challenging Glass Conference Proceedings; 2016.
[42] Bradt RC. Glass fracture patterns and the (G,R) vs Delta C diagram. J Non-Cryst Solids. 2012;358(24):3459-64. https://doi.org/10.1016/j.jnoncrysol.2012.01.067.
[43] Bradt RC. Applying fractography and fracture mechanics to the energy and mass of crack growth for glass in the mirror region. J Eur Ceram Soc. 2014;34(14):3255-62. https://doi.org/10.1016/j.jeurceramsoc.2014.04.036.
[44] Wiederhorn SM. Fracture surface energy of glass. J Am Ceram Soc. 1969;52(2):99-105. https://doi.org/10.1111/j.1151-2916.1969.tb13350.x.
[45] OKAFOR C, Martin DM. The Effect of Temperature on the Fracture‐Surface Energy of A Waste Disposal Glass. J Am Ceram Soc. 1982;65(2):87-90. https://doi.org/10.1111/j.1151-2916.1982.tb10363.x.
[46] Jensen HM. Crack initiation and growth in brittle bonds. Eng Fract Mech. 2003;70(13):1611-21. https://doi.org/10.1016/S0013-7944(02)00200-X.
[47] Aguiar AR, Patriota TV. Brittle Fracture Modeling Using Ordinary State-Based Peridynamics with Continuous Bond-Breakage Damage. J Peridyn Nonlocal Model. 2021:1-40. https://doi.org/10.1007/s42102-021-00057-y.
[48] Rouxel T. Fracture surface energy and toughness of inorganic glasses. Scr Mater. 2017;137:109-13. https://doi.org/10.1016/j.scriptamat.2017.05.005.
[49] Illian J, Penttinen A, Stoyan H, Stoyan D. Statistical analysis and modelling of spatial point patterns: John Wiley & Sons; 2008.
[50] Baddeley A, Rubak E, Turner R. Spatial point patterns: methodology and applications with R. New York: CRC press; 2015. https://doi.org/10.1201/b19708.

[51] Cook RL. Stochastic sampling in computer graphics. ACM Trans Graph. 1986;5(1):51–72. https://doi.org/10.1145/7529.8927.
[52] Grekousis G. Spatial Analysis Methods and Practice: Describe – Explore – Explain through GIS. Cambridge: Cambridge University Press; 2020. https://doi.org/10.1017/9781108614528.
[53] Bivand RS, Pebesma EJ, Gómez-Rubio V. Applied spatial data analysis with R. New York: Springer; 2013. https://doi.org/10.1007/978-1-4614-7618-4.
[54] Ren N, Shang B, Guan P, Hu L. General structural and dynamic characteristics beneficial to glass-forming ability of Fe-based glass-forming liquids. J Non-Cryst Solids. 2018;481:116-22. https://doi.org/10.1016/j.jnoncrysol.2017.10.029.
[55] Kim K, Rutqvist J, Nakagawa S, Birkholzer J. TOUGH–RBSN simulator for hydraulic fracture propagation within fractured media: Model validations against laboratory experiments. Comput Geosci. 2017;108:72-85. https://doi.org/10.1016/j.cageo.2017.05.011.
[56] Hirobe S, Imakita K, Aizawa H, Kato Y, Urata S, Oguni K. Mathematical model and numerical analysis method for dynamic fracture in a residual stress field. Phys Rev E. 2021;104(2):025001. https://doi.org/10.1103/PhysRevE.104.025001.
[57] Green PJ, Sibson R. Computing Dirichlet tessellations in the plane. The computer journal. 1978;21(2):168-73. https://doi.org/10.1093/comjnl/21.2.168.
[58] Moller J. Lectures on random Voronoi tessellations. New York: Springer New York; 1994. https://doi.org/10.1007/978-1-4612-2652-9.
[59] Aurenhammer F, Klein R. Voronoi Diagrams. In: Sack J-R, Urrutia J, editors. Handbook of computational geometry. Amsterdam, Netherlands; 2000. p. 201-90.
[60] Burrough PA, McDonnell RA, Lloyd CD. Principles of geographical information systems: Oxford university press; 2015.
[61] Lucarini V. From symmetry breaking to Poisson point process in 2D Voronoi tessellations: the generic nature of hexagons. J Stat Phys. 2008;130(6):1047-62. https://doi.org/10.1007/s10955-007-9475-x.

CRediT authorship contribution statement

Yuhan Zhu: Writing - original draft, Investigation, Data curation, Software. **Jian Yang**: Writing - review & editing, Funding acquisition. **Xing-er Wang**: Writing - review & editing, Supervision, Funding acquisition. **Dongdong Xie**: Data curation, Validation. **Xiaonan Hou**: Writing - review & editing.

Declaration of interests

☒The authors declare that they have no known competing financial interests or personal relationships that could have appeared to influence the work reported in this paper.

☐The authors declare the following financial interests/personal relationships which may be considered as potential competing interests: